Impact of dynamic desiccation cracks on hydrological processes and stability in expansive clay slopes

A coupled dual-permeability modeling approach

Luo, Yi; Zhang, Jiaming; Tang, Chao Sheng; Jiang, Guosheng; Bogaard, Thom

DOI
10.1016/j.enggeo.2025.108377

Publication date
2025

Document Version
Final published version

Published in
Engineering Geology

Citation (APA)
Luo, Y., Zhang, J., Tang, C. S., Jiang, G., & Bogaard, T. (2025). Impact of dynamic desiccation cracks on hydrological processes and stability in expansive clay slopes: A coupled dual-permeability modeling approach. *Engineering Geology*, *357*, Article 108377. https://doi.org/10.1016/j.enggeo.2025.108377

Engineering Geology 357 (2025) 108377

Contents lists available at ScienceDirect

Engineering Geology

journal homepage: www.elsevier.com/locate/enggeo

Impact of dynamic desiccation cracks on hydrological processes and stability in expansive clay slopes: A coupled dual-permeability modeling approach

Yi Luo [a,b], Jiaming Zhang [b,*], Chao-Sheng Tang [c], Guosheng Jiang [b], Thom Bogaard [d]

[a] School of Urban Construction, Wuhan University of Science and Technology, Wuhan 430065, China
[b] Faculty of Engineering, China University of Geosciences (Wuhan), 388 Lumo Avenue, Wuhan 430074, China
[c] School of Earth Sciences and Engineering, Nanjing University, 163 Xianlin Road, Nanjing 210023, China
[d] Water Resources Section, Faculty of Civil Engineering and Geosciences, Delft University of Technology, Stevinweg 1, P.O. Box 5048, 2600 GA Delft, the Netherlands

ARTICLE INFO

Keywords:
Desiccation crack dynamics
Preferential flow
Dual-permeability model
Slope hydrology
Slope stability

ABSTRACT

Preferential flow and soil strength degradation induced by desiccation cracks are important causes for expansive clay slope instability. The cyclic opening and closing of desiccation cracks during drying-wetting processes incessantly alters preferential flow paths and soil strength. Quantify the impact of desiccation crack dynamics on slope hydrology and stability remains a major unresolved challenge. To bridge this gap, we developed the first slope-scale hydro-mechanical model that couples weather-driven crack evolution with preferential flow while incorporating the deterioration effect on soil strength. This unified approach is a major contribution to our capacity to model the integration of hydrological processes and mechanical degradation of soil strength induced by dynamic cracks. The hydrological part adopted a dynamic dual-permeability model (dynamic DPM) and was validated by a physical slope model test. The dynamic DPM was then integrated into a set of numerical slope stability analyses under one-year atmospheric conditions. The groundwater level, water balance, pore water distribution, crack evolution and slope stability were investigated in the case of dynamic cracks and fixed cracks. The hydrological results showed that the slope model with dynamic cracks retained more water and higher groundwater level than that with fixed cracks. The narrowing of desiccation cracks slows down slope drainage process, resulting in a rapid build-up of pore water pressure due to preferential flow, which emerges as an often overlooked and significant factor contributing to slope instability. Conversely, fixed and well-connected cracks in soils enhance water drainage and thus benefit slope stability. The mechanical results revealed that the irreversible deterioration effect induced by crack dynamics on soil strength persistently degrades long-term slope stability. These findings provide new insights into failure mechanisms in cracked soil slopes, and show the importance of the integration of dynamic crack properties into climate-resilient slope design. Also, our results underscore the importance of understanding and quantifying the physical behavior of soil structures for soil hydrological response and slope stability assessment.

1. Introduction

Desiccation cracks, resulting from soil shrinkage during drought or drying-wetting cycles, are ubiquitously developed in expansive clays (Tang et al., 2011; Xu et al., 2024; Yang et al., 2025). As shown in Fig. 1, these cracks show cyclic opening and closure process under drying-wetting cycles, serving as dual agents of preferential flow pathways (Beven and Germann, 1982; Bradley et al., 2007; Greve et al., 2010; Luo et al., 2025; Yuliana et al., 2025; Tang et al., 2024) and progressive soil strength degradation (Stirling et al., 2021; Take and Bolton, 2011; Xu et al., 2021; Zhan et al., 2013). Such hydromechanical alteration is widely acknowledged as a critical hydrological precursor to slope instability and shallow landslides in expansive clays (Bogaard and Greco, 2015; Caris and Van Asch, 1991; Gao et al., 2023; Greco et al., 2023; Luo et al., 2021; Zhang et al., 2021a). With rising global temperatures worsening both droughts and storms (Chaduvula et al., 2022; Vahedifard et al., 2020), the coupling of preferential flow and crack strength deterioration poses escalating threats to slope stability

* *Corresponding author.
E-mail address: zjm@cug.edu.cn (J. Zhang).

https://doi.org/10.1016/j.enggeo.2025.108377
Received 31 March 2025; Received in revised form 15 August 2025; Accepted 21 September 2025
Available online 24 September 2025

(Tichavsky et al., 2019), yet the hydro-mechanical effects of desiccation crack dynamics on slope hydrology and stability remain poorly understood and quantified.

The key to addressing the aforementioned gaps lies in developing an advanced slope hydro-mechanical model. One major challenge is how to develop a hydrological model capable of simulating the reciprocal interactions between desiccation crack evolution and slope hydrology. Previous efforts have been devoted to employ explicit crack models (Chen et al., 2024; Gao et al., 2025; Khan et al., 2017; Pei et al., 2020; J Zhang et al., 2020) and implicit crack models (Dusek et al., 2012; Han et al., 2025; Hopp et al., 2020; Shao et al., 2015) to simulate hydrological process in slopes with macropores (e.g. desiccation cracks). Explicit models define crack geometry and properties in detail (Pei et al., 2020; Reeves et al., 2014) and offer physical fidelity but face computational limitations at larger scales or for extensive crack networks (Aguilar-López et al., 2020; Luo et al., 2023a, 2023b). Advanced nonlocal approaches such as phase-field methods (Zhuang et al., 2021, 2022) and peridynamics (Altay et al., 2024; Dorduncu et al., 2022a, 2022b, 2024) provide alternatives for crack modeling but require complex implementation and parameterization for hydromechanical coupling. Meanwhile, prevailing explicit crack models treat cracks as isolated, disconnected and fixed line conduits, neglecting the desiccation crack dynamics. Implicit crack models treat the soil as overlapping regions representing the matrix and macropores (e.g. desiccation cracks). These models implicitly represent soil cracks, obviating the need to define the geometric and spatial characteristics of desiccation cracks explicitly. The most well-known one is the classical dual-permeability model (DPM) (Aguilar-López et al., 2020; Gerke and Maximilian Köhne, 2004; Gerke and van Genuchten, 1993; Larsbo and Jarvis, 2003; Šimůnek et al., 2003), which has garnered widespread acceptance due to its accessible parameters, reasonably satisfactory predictions, and low computational burden (Jarvis et al., 2016). Nevertheless, classical DPMs assume fixed crack volumes and hydraulic properties, also limiting their ability to capture crack dynamic processes during drying-wetting cycles.

A second challenge lies in the mechanical component of hydro-mechanical slope stability models. Conventional slope stability models often assume constant soil mechanical parameters (Chen et al., 2024; Gao et al., 2025; Shao et al., 2018; Sun et al., 2019), overlooking soil strength degradation from crack-induced fabric damage (e.g., bond breakage and pore reorganization) during cyclic wetting-drying (Stirling et al., 2021; Take and Bolton, 2011; Zhan et al., 2013). While nonlocal operator methods show promise for crack propagation modeling (Zhuang et al., 2021; Dorduncu et al., 2022a), their application to cyclic strength degradation in unsaturated soils remains underdeveloped. Empirical functions have been proposed to link bulk soil strength with wetting-drying cycles (Gao et al., 2021; Xue et al., 2022), their applicability is constrained by spatial heterogeneity of crack status and varying wetting-drying paths under realistic atmospheric conditions. Peridynamic frameworks for functionally graded materials (Dorduncu et al., 2022b) and fatigue analysis (Altay et al., 2024) offer insights for damage evolution modeling, yet lack integration with hydrological processes. A simple and fundamental solution may involve developing a function that links crack development status to soil mechanical parameters (Chen et al., 2025; Jamalinia et al., 2020). However, due to the complex spatiotemporal dynamics of desiccation cracks in response to moisture variations (Cheng et al., 2021; Tang et al., 2011; Tian et al., 2022; Xu et al., 2022; Zeng et al., 2021), the absence of an effective hydrological model capable of simulating crack dynamics critically impedes the practical implementation of such functions.

This study aims to understand and quantify the effects of desiccation crack dynamics on slope hydrology and stability. A dynamic dual-permeability model (DPM) was developed by integrating crack-permeability dynamic functions into conventional dual-permeability

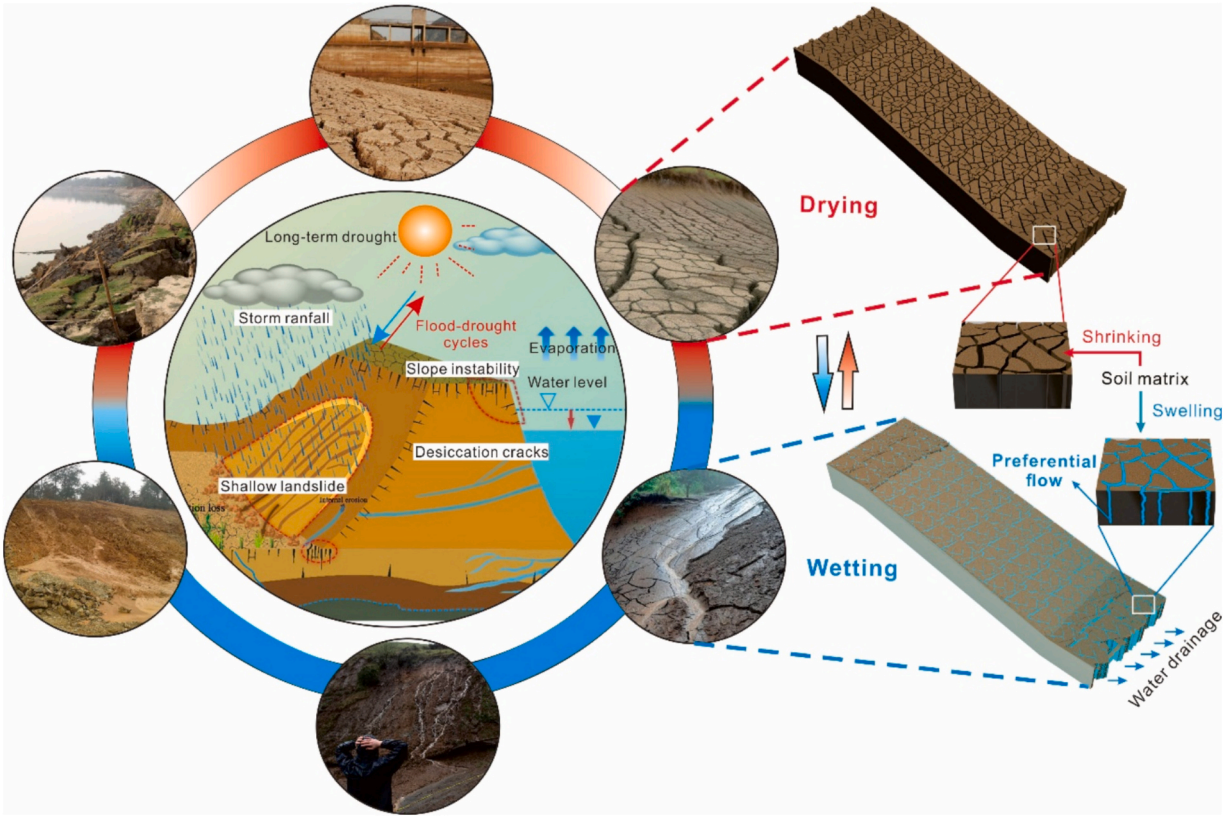

Fig. 1. Slope instability related to desiccation crack dynamics (left part) (the circular animated schematic was adapted from Tang et al. (2021)) and preferential flow through desiccation cracks in cracked slope (right part).

model. The dynamic DPM can simulate desiccation crack dynamics and its influence on soil water flow under atmospheric forcing, and it was then validated using data from a physical slope experiment. Subsequently, we established a hydro-mechanical framework that couples the dynamic DPM with a strength degradation function linked to crack development. Finally, through numerical experiments on a synthetic slope under realistic atmospheric conditions, we systematically compared the slope hydrology (groundwater level, water balance, pore pressure distribution) and stability between dynamic and fixed crack scenarios.

2. Theoretical model description

As illustrated in Fig. 2, modeling water movement in cracked soil during drying-wetting cycles requires quantifying three key physical processes: (i) water flow within the crack and matrix domains and the water transfer between these domains during evaporation and infiltration; (ii) the coupled evolution of matrix pores and desiccation cracks driven by soil shrink-swell behavior; and (iii) changes in hydraulic conductivity within the matrix and crack domains resulting from the pore-crack interaction. These interconnected processes impose mutual constraints, necessitating the use of physically-based equations that are both independent and capable of coupling.

To achieve this, this study employs the dual-permeability model (DPM) with implicit crack characteristics. For fixed cracks, the classical/rigid dual-permeability model (rigid DPM) is applied, effectively capturing the processes described in (i). For dynamic desiccation cracks, the rigid DPM is extended by incorporating functions represent crack dynamics and changes in permeability within the two domains, forming a dynamic dual-permeability model (dynamic DPM). This approach enables the simultaneous description of processes (i), (ii) and (iii). Note that this study does not consider the effects of changes in soil-water retention properties, heat transfer, or water-vapor transmission on soil structural dynamics.

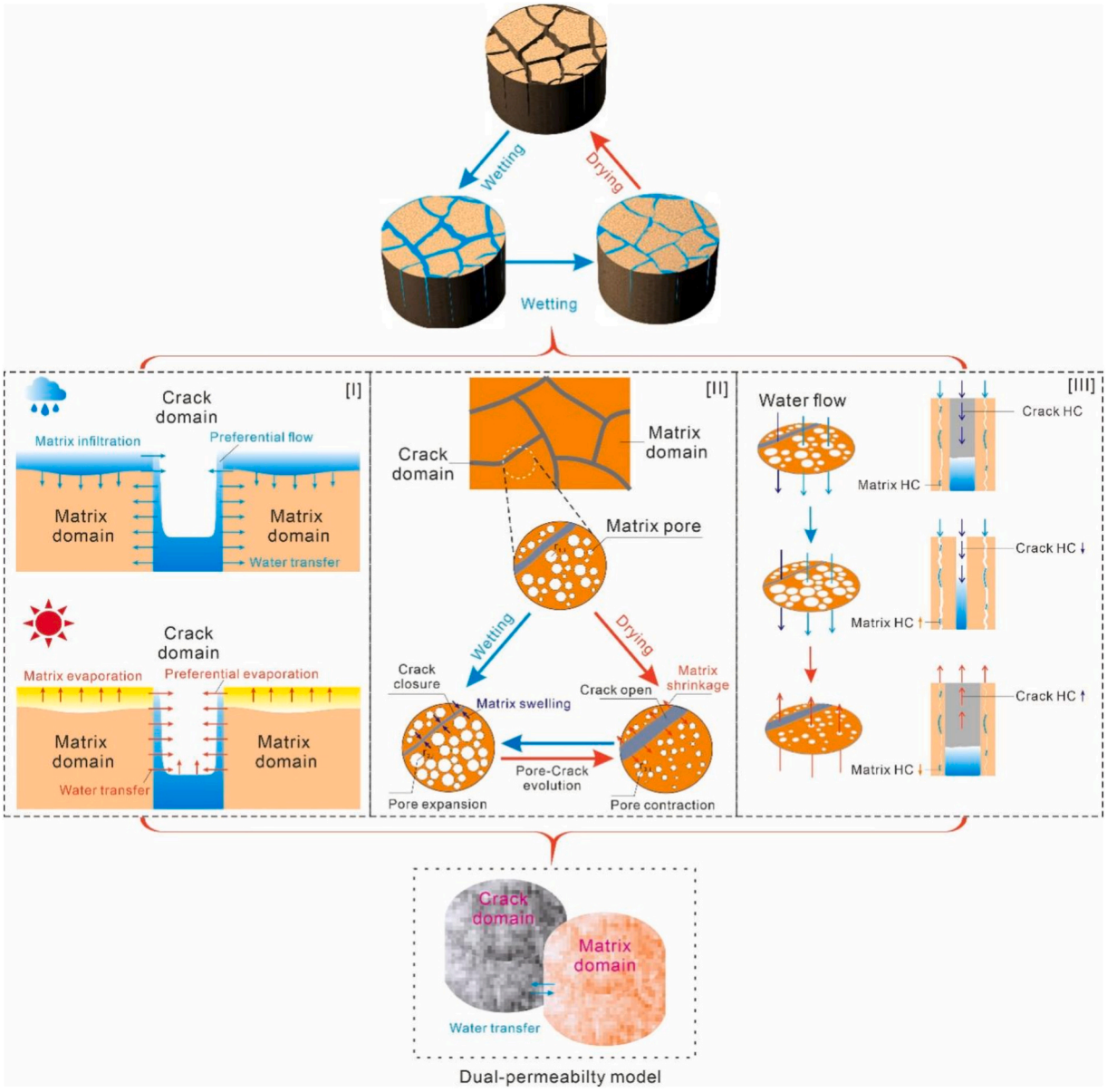

Fig. 2. Schematic diagram illustrating the three physical process related to the water movement in the cracked clay (*HC: Hydraulic conductivity) (I) Water flow and transfer in and between the crack and matrix domains; (II) desiccation crack dynamics caused by soil shrink-swell behavior; (III) changes of hydraulic properties caused by crack dynamics.

2.1. Rigid dual-permeability model (rigid DPM) for preferential flow in fixed cracks

In this work, the classical/rigid dual-permeability model (rigid DPM) developed by Gerke and van Genuchten (1993) was adopted to simulate preferential flow through soils with fixed cracks. As shown in Fig. 2, the model delineates the soil into two interdependent continua, each characterized by distinct volumetric ratios. This approach modifies Richards' equations to describe fluid movement through both the soil matrix and the preferential flow paths. The equation express of fluid flow within each continuum as follows:

For the crack domain:

$$C_c(h)\frac{\partial h_c}{\partial t} = \nabla[-K_c(h)\nabla(h_c+z)] - \frac{\Gamma_w}{w_c} \tag{1}$$

For the matrix domain:

$$C_m(h)\frac{\partial h_m}{\partial t} = \nabla[-K_m(h)\nabla(h_m+z)] + \frac{\Gamma_w}{w_m} \tag{2}$$

Here, Γ_w denotes the water transfer between domains:

$$\Gamma_w = \alpha_w K_a(h_c - h_m) \tag{3}$$

The balance of volumetric ratios is given by:

$$w_c + w_m = 1 \tag{4}$$

The total water content θ and hydraulic conductivity K in the composite medium are defined as:

$$\theta = w_c\theta_c + w_m\theta_m \tag{5}$$

$$K = w_cK_c + w_mK_m \tag{6}$$

The notations are as follows: "c" and "m" are the abbreviation of the crack and matrix domains, respectively, w is the volumetric ratio (−), h is the pressure head (m), C is the specific water capacity $\mathrm{d}\theta/\mathrm{d}h$ (1/m), K is the isotropic hydraulic conductivity (m/s), z is the elevation head (m), Γ_w is the inter-domain water exchange term (1/s), α_w represents water transfer coefficient (1/m^2), K_a is the interface hydraulic conductivity (m/s). The total volumetric moisture content, θ, reflects the combined moisture levels in both domains.

The α_w can be calculated as

$$\alpha_w = \frac{\beta\gamma_w}{a^2} \tag{7}$$

where β represents a dimensionless shape factor that is determined by the soil matrix configuration. It has been standardized to a value of 3 as per Aguilar-López et al. (2020), γ_w denotes a dimensionless scaling coefficient recommended to be 0.4 (Gerke et al., 2007), and a serves as a scaling factor, correlating roughly to half of the matrix's width (m), which can be determined experimentally.

The dual-permeability model further incorporates an improved K_a function revised by Gerke et al. (2013), which expressed as

$$K_{a_{\min}} = \begin{cases} \min\{K_m(h_c), K_c(h_c)\} & h_c \geq h_m \\ \min\{K_m(h_m), K_c(h_m)\} & h_c < h_m \end{cases} \tag{8}$$

This equation models fluid movement from regions of higher hydraulic head to those of lower, governed by the less permeable domain at a given moment (Aguilar-López et al., 2020).

The hydraulic properties (soil-water retention and hydraulic conductivity functions) of each domain are described based on the Mualem-van Genuchten function (Mualem, 1976; van Genuchten, 1980) as

$$S_e(h) = \frac{\theta-\theta_r}{\theta_s-\theta_r} = [1+(|\alpha h|)^n]^{(n-1)/n} \tag{9}$$

$$K_m(S_{e,m}) = K_{m,s}K_r(S_{e,m}) = K_{m,s}S_{e,m}{}^{0.5}\left[1-\left(1-S_{e,m}{}^{n_m/(n_m-1)}\right)^{(n_m-1)/n_m}\right]^2 \tag{10}$$

$$K_c(S_{e,c}) = K_{c,s}K_r(S_{e,c}) = K_{c,s}S_{e,c}{}^{0.5}\left[1-\left(1-S_{e,c}{}^{n_c/(n_c-1)}\right)^{(n_c-1)/n_c}\right]^2 \tag{11}$$

where θ_s(−) and θ_r (−) are the saturated and residual volumetric moisture content, respectively; α(1/m) and n(−) are fitting parameters; K_r (−) represents the relative hydraulic conductivity. Note that the $K_{m,s}$ and $K_{c,s}$ are fixed in rigid DPM.

For the dual-permeability model, the flux partitioning is given by the relation:

$$i = w_ci_c + w_mi_m \tag{12}$$

where i_c and i_m are the effective domain-specific boundary fluxes (m/s).

Under rainfall conditions, the initial effective boundary flux for both soil domains is set to be equal to rainfall intensity (r) (Dusek et al., 2008), and the boundary fluxes can be expressed as

$$i_c = r \tag{13}$$

$$i_m = r \tag{14}$$

With ongoing rainfall, the infiltration capacity of the matrix domain may fall below the rainfall intensity r, resulting in ponding. At this moment, the boundary condition changes to a pressure head boundary. When ponding initiates in the matrix domain, the surface runoff shifts into the crack domain, prompting an increase in flux i_c as follow:

$$i_c = (r\text{-}w_mi_m)/w_c \tag{15}$$

If the water stored within the cracks surpasses its retention capacity, surface ponding occurs in the crack domain as well.

To model the evaporation from each domain during dry periods, the study employs the Wilson-Forchheimer-Darcy model (Wilson et al., 1997) to estimate the actual evaporation rate, which is expressed as:

$$AE\Big/PE = \exp\left(\frac{-Sg\omega_v}{\xi(1-h_a)\gamma_wR(273.15+T_s)}\right) \tag{16}$$

where, AE represents the actual evaporation; PE denotes the measured potential evaporation; S is the matric suction of the soil surface (kPa). The constant g refers to gravitational acceleration (m/s^2); ω_v has a value of 0.018 kg/mol and is the molecular mass of water; ξ is a dimensionless empirical parameter, with a recommended value of 0.7; h_a signifies the relative humidity of the overlying air; γ_w is the unit mass of water, equivalent to 9.807 kN/m^3; R is the universal gas constant, valued at 8.314 J/(mol·K); T_s (°C) indicates the temperature of soil surface.

2.2. Dynamic dual-permeability model (dynamic DPM) for preferential flow in desiccation cracks

During the opening and closing process of desiccation cracks, the proportion (or volume) and hydraulic conductivity of each domain vary with moisture content of the matrix domain. Therefore, the key problem of developing a dynamic DPM is how to describe the changes of w_c, w_m, K_m and K_c responding to the matrix moisture content. Building on the rigid DPM, a physically-based soil shrinking-swelling model and two dual-domain infiltration functions proposed by Stewart et al. (2016b); (Stewart et al., 2016a) were incorporated to form a dynamic DPM. The dynamic DPM can well describe the variation of porosity, volumetric ratio and hydraulic conductivity of the matrix and crack domains, which mainly includes four core equations as follows.

$$\phi_{matrix}(S_{e,m}) = (\phi_{\max}-\phi_{\min})\left(\frac{p+1}{p+S_{e,m}{}^{-q}}\right)+\phi_{\min} \tag{17}$$

$$K_{m,s}(S_{e,m}) = K_{m,\max}\left(\frac{p+1}{p+S_{e,m}^{-q}}\right) \tag{18}$$

$$w_c(S_{e,m}) = (\phi_{\max}-\phi_{\min})\left(\frac{1-S_{e,m}^{q}}{1+pS_{e,m}^{q}}\right)+w_{c,\min} \tag{19}$$

$$K_{c,s}(S_{e,m}) = K_{c,\max}\left(\frac{1-S_{e,m}^{q}}{1+pS_{e,m}^{q}}\right)^{2}+K_{c,\min} \tag{20}$$

where ϕ_{matrix} is the matrix porosity; $\phi_{\max}$, $\phi_{\min}$, p and q are shrinking-swelling parameters (Luo et al., 2023a); $K_{m,\max}$ is the maximum saturated hydraulic conductivity of the matrix domain (at $S_{e,m}=1$); $K_{c,\max}$ is the maximum saturated hydraulic conductivity of the crack domain (at $S_{e,m}\approx 0$); $w_{c,\min}$ is the minimum crack proportion due to incomplete crack closure process, approximately be 0.01 (2015; Coppola et al., 2012, 2015; Luo et al., 2023a); $K_{c,\min}$ is the minimum saturated hydraulic conductivity of the crack domain corresponds to the $w_{c,\min}$ (at $S_{e,m}\approx 1$).

The study diverges from rigid DPM by amending Eqs. (10) and (11) to incorporate the dynamics of $K_{m,s}$ and $K_{c,s}$ related to matrix pore and crack shrink-swell behavior. Additionally, the $K_r(S_{e,c})$, is set to 1 in Eq. (11), ensuring that K_c is a function of crack aperture rather than the saturation degree of that domain ($S_{e,c}$), thus preventing unfeasibly low K_c under dry conditions or prolonged desiccation.

$$\begin{aligned} K_m(S_{e,m}) &= K_{m,s}(S_{e,m})K_r(S_{e,m}) \\ &= K_{m,\max}\left(\frac{p+1}{p+S_{e,m}^{-q}}\right)S_{e,m}^{0.5}\left[1-\left(1-S_{e,m}^{n_m/(n_m-1)}\right)^{(n_m-1)/n_m}\right]^{2} \end{aligned} \tag{21}$$

$$K_c = K_{c,s}(S_{e,m}) = K_{c,\max}\left(\frac{1-S_{e,m}^{q}}{1+pS_{e,m}^{q}}\right)^{2}+K_{c,\min} \tag{22}$$

For more details on the validation and sensitive analysis of the dynamic DPM, please refer to our prior works (Luo et al., 2023a, 2023b).

3. Description of the physical slope model test

In our earlier work (Luo et al., 2023a), the aforementioned dynamic DPM was validated through soil column experiments dominated by vertical infiltration. However, its applicability to slopes with significant lateral preferential flow remains untested. To address this gap, we conducted novel rainfall-evaporation experiments on a pre-desiccated slope model featuring stabilized crack networks (developed over 6 months). This setup enabled validation of dynamic DPM under lateral flow regimes. The 1.5 m × 0.5 m × 0.25 m slope (15° incline) used compacted expansive clay, with instrumentation monitoring crack dynamics, pore pressure, and boundary flows (Fig. 3). Gentle slope geometry ensured hydrology was dominated by desiccation cracks rather than mechanical failure. Further details, including soil properties and measurement methods, can be found in our recent work (Luo et al., 2025).

The first-stage experiment ran from March 12 (11:21) to June 20, 2024 (15:00), completing ten drying-wetting cycles. The primary objective of this stage was to develop a stable desiccation crack network penetrating the entire slope depth (as shown in Fig. 3c), which is a crucial prerequisite for applying the dynamic DPM (Luo et al., 2023a; Luo et al., 2023b). Following the first-stage experiment, a five-hour rainfall event was applied, with an intensity of approximately 30 mm/h and a total rainfall of 150 mm. A subsequent three-day evaporation

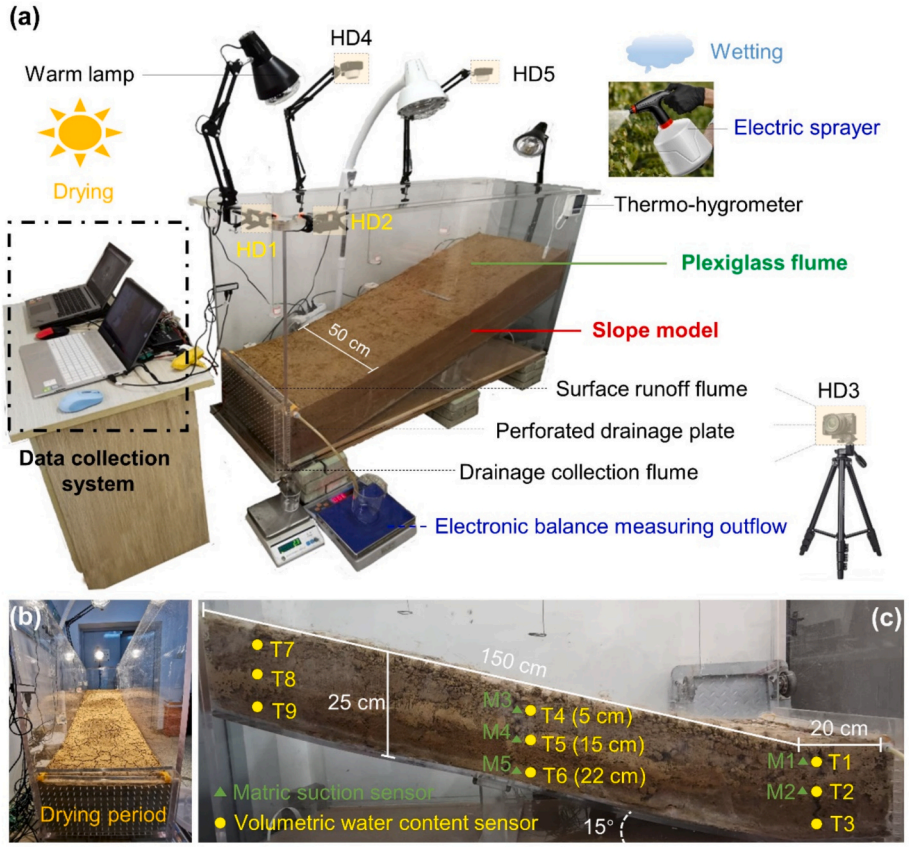

Fig. 3. Experimental configuration of instrumented expansive clay slope: (a) Components of the model test system; (b) slope model during drying period; (c) hydrological sensors deployment.

phase maintained an average rate of 0.2 mm/h. Then, another five-hour rainfall event with the same intensity (30 mm/h) and total rainfall (150 mm) was applied. Finally, two-day natural evaporation period with average evaporation rate of 0.05 mm/h was applied.

Fig. 4 presents how rainfall, evaporation, temperature and humidity changed over the experiment period.

4. Model verification

As shown in Fig. 5, a 2D numerical slope model consistency with the physical slope experiment was established in COMSOL to validate the proposed theoretical model. Both the rigid DPM and dynamic DPM were incorporated for comparative analysis. The numerical slope model was divided into a crack domain and a matrix domain, both sharing the same mesh structure, boundary conditions and initial conditions. These two domains also shared identical mesh nodes, with boundary flow distribution governed by Eq. (15) and water exchange determined by Eq. (8). The upper boundary of the model was defined as a rainfall-ponding-evaporation boundary, consistent with the experimental boundary conditions. The left boundary was set as a seepage boundary, while the bottom and right boundaries were designated as impermeable boundaries. To better capture the frequent variations in climatic boundary conditions, the surface layer mesh was refined. This layer consisted of 15 layers of triangular elements, with thickness ranging from approximately 0.04 cm to 0.3 cm. Underlying this layer, a coarsened free-triangle grid (mean element size = 1.8 cm) was implemented. The total number of mesh elements is 1496, with an average element area of 2.75 cm^2. The initial conditions were derived from the measured matric suction before the experiment began, with an average value of approximately −60 kPa. To ensure numerical robustness, mesh independence was confirmed through sensitivity tests with average element sizes of 0.83 cm^2 and 7.15 cm^2. Adaptive time-step method was used with free step size control. Convergence was controlled by relative and absolute tolerances of 0.01 and 1×10^{-5} kPa, respectively. The absolute tolerance factor was kept at 1.0 to ensure consistent thresholds across varying pressure magnitudes.

The rigid DPM requires 12 parameters to be determined, whereas the dynamic DPM requires 17 parameters. These parameters are obtained through experiments and empirical values and can be categorized into three main aspects:

(i) **Water transfer coefficient** (α_w): As shown in Fig. 6, the mean soil matrix width measured in the slope model test is approximately 44 mm. As defined in Eq. (7), the characteristic length a is set to be 22 mm, and α_w is calculated as 2479 $1/m^2$.

(ii) **Soil shrink-swell parameters:** For the dynamic DPM, the shrink-swell parameters mainly refer to the four shrinkage curve parameters in Eq. (17), which were calibrated against the measured soil shrinkage curves under similar dry density conditions as the model experiment (Fig. 7a). Subsequently, the variation of crack ratio versus matrix saturation degree was obtained using Eq. (19). For the rigid DPM, as the effects of soil matrix swelling are not considered, w_c was fixed based on the initial surface crack ratio observed before the experiment, set at 0.3.

(iii) **Hydraulic property parameters for both rigid and dynamic DPMs:** These include the soil-water retention curve (SWRC) and hydraulic conductivity. For the matrix domain, SWRC parameters were obtained through pressure plate experiments using seven equilibrium matric suctions (0, 10, 30, 50, 100, 150, 200, 300, and 500 kPa). The distributed soil samples (20 mm × 61.4 mm) with void ratio of 1.10 (ρ_d=1.3 g/cm^3, matching the model slope) were saturated using the vacuum pumping method before being placed in the pressure vessel. The fitted SWRC curve using Eq. (9) is shown in Fig. 7b. For the crack domain, assuming no solid material within the cracks, the saturated water content ($\theta_{c,s}$) and the residual water content ($\theta_{c,s}$) of that domain was set to be 0.99 and 0.01, respectively, based on Aguilar-López et al. (2020). Since the SWRC of the crack domain cannot be experimentally determined, the remaining parameters ($a = 1.5$ and $n_c = 3$) were assigned to mimic the behavior of coarse-textured soils. This follows the Poiseuille law, implying minimal capillary effects on water flow through cracks.

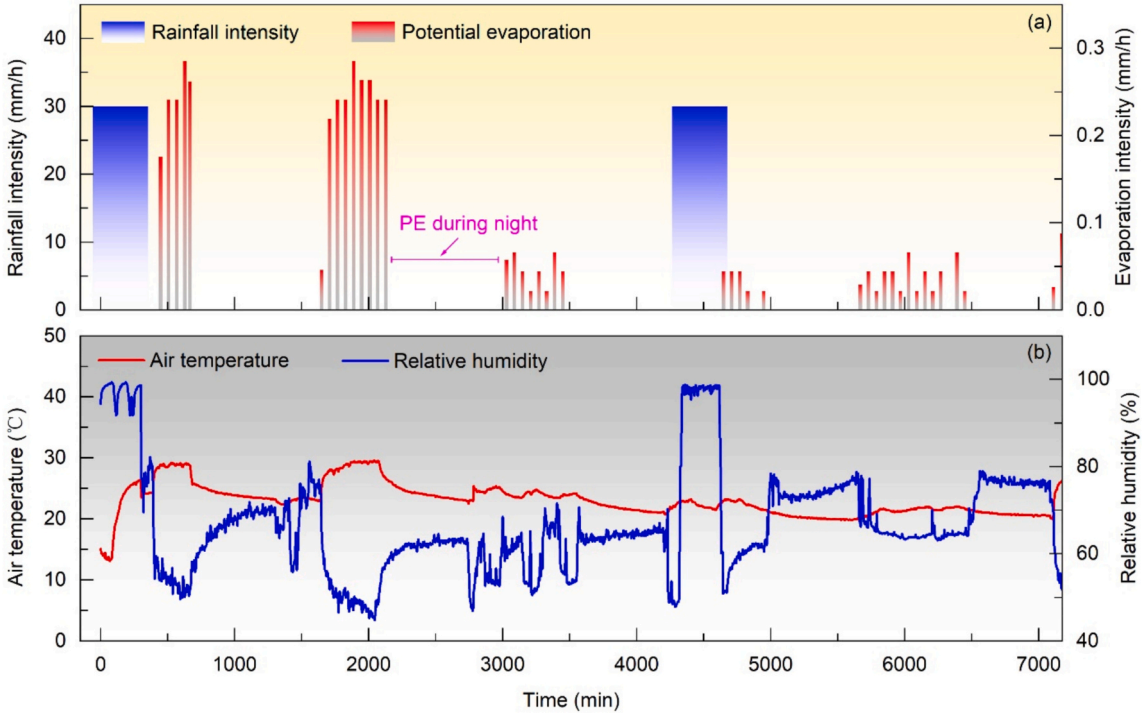

Fig. 4. Boundary environmental records

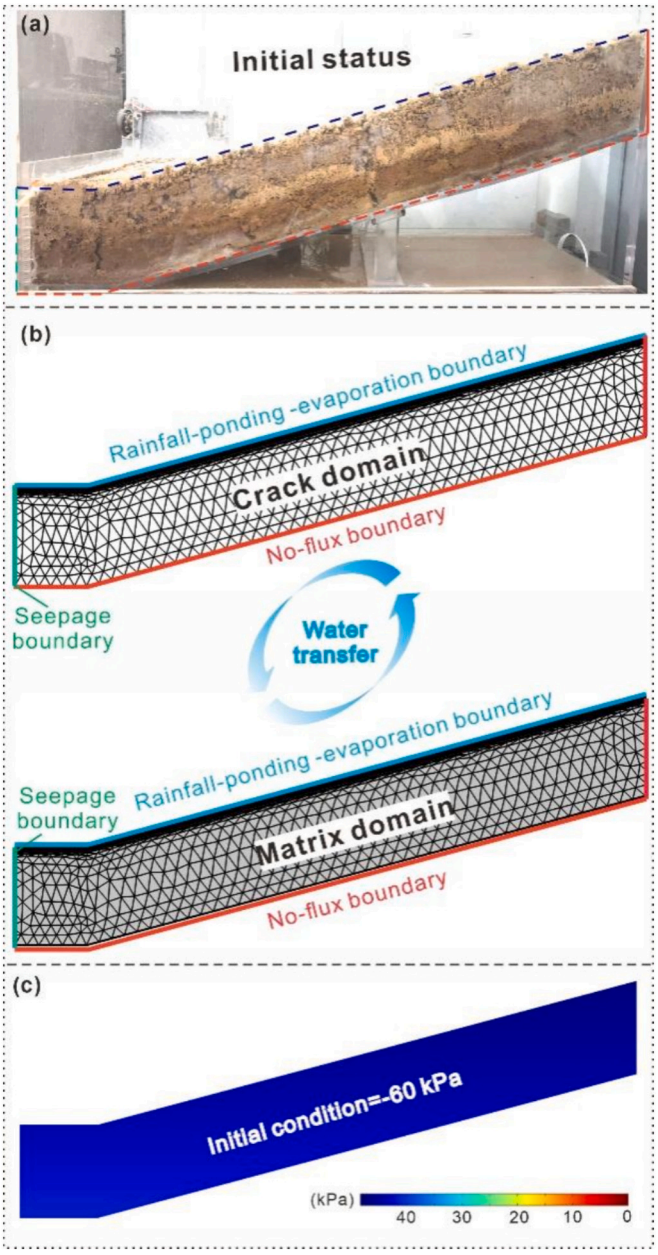

Fig. 5. Set-up of the numerical model and parameterization.

The maximum saturated hydraulic conductivity of matrix domain ($K_{m,\max}$) was measured under dry density of 1.3 g/cm^3 using constant-head method in which the hydraulic head gradient was kept at 15 kPa. The $K_{m,\max}$ was measured to be 2.6 × 10^{-6} m/s. Regarding the $K_{c,\max}$, it was calculated using Hagen-Poiseuille equation (SNOW, 1965) based on the maximum crack aperture.

$$K_c = \frac{w_j^2 g}{12\nu} \tag{23}$$

where w_j refers to the observable crack aperture from experimental or field measurements (m), and ν is the water kinematic viscosity (m^2/s). From slope model test (Luo et al., 2025), the $w_{j,\max}$ was measured to be 3.8 mm. Then, as shown in Fig. 7c, the hydraulic conductivity curves of the matrix and crack domains in both rigid and dynamic DPMs were derived using Eqs. (10)–(11) and Eqs. (21)–(22), respectively.

The summary of parameters is listed in Table 1.

Fig. 8 compares the measured surface crack ratio at different slope locations with the simulated results from the dynamic DPM and Table. 2 gives the statistical error measures. The results indicate that the observed crack ratio sharply decreases to near zero during rainfall and gradually increases during drying. Due to the higher evaporation intensity in the first drying phase compared to the second, the crack ratio exhibits a more significant increase in the first drying phase. Overall, the dynamic DPM closely matches the measured crack ratio in both trend and magnitude. However, a slight underestimation is observed for the crack ratio in the mid-slope region during drying. It can be attributed to higher localized evaporation from intensive lamp heating (see Fig. 3) not fully captured by the uniform boundary approximation. Fig. 9 presents a comparison of the measured volumetric water content and matric suction at different depths of the slope toe and mid-slope with the simulation results from both the dynamic DPM and rigid DPM. Table. 3 gives the statistical error measures involving the volumetric water content and matric suction. The trends show that the volumetric water content follows a similar pattern to the crack ratio, while matric suction exhibits an inverse relationship. Overall, the dynamic DPM provides accurate predictions for both matric suction and volumetric water content, whereas the rigid DPM significantly overestimates matric suction and underestimates volumetric water content. Fig. 10 further compares the measured and simulated lateral discharge rates of the slope. The results indicate that the observed discharge rate exhibits a sharp increase followed by a gradual decline during both rainfall events, which aligns well with the simulated discharge rate from the dynamic DPM. This finding suggests that during the later stages of rainfall, as cracks gradually close, the slope's discharge capacity is also suppressed. Although some deviations exist between the simulated and measured discharge rates, the discrepancy remains acceptable. In contrast, the rigid DPM greatly overestimates slope discharge—exceeding the actual value by more than 20 times (not shown in Fig. 11 due to excessive deviation). This also explains why the rigid DPM underestimates volumetric water content across the slope.

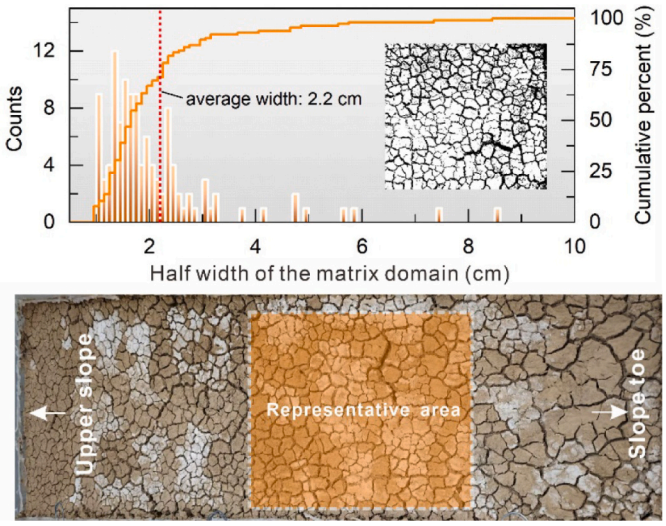

Fig. 6. Determination of the half matrix width through statistical histogram.

5. Numerical experiments considering slope stability

The previous study has demonstrated the effectiveness and accuracy of the dynamic DPM in simulating desiccation crack dynamics and associated slope hydrology. However, due to the scale effects of the small-scale model test and the limited test duration, the impact of crack dynamics on slope stability remains insignificant. Therefore, this section focuses on developing a hydro-mechanical model based on the dynamic DPM to investigate the influence of desiccation crack dynamics on slope hydrology and stability under real slope-scale conditions and actual

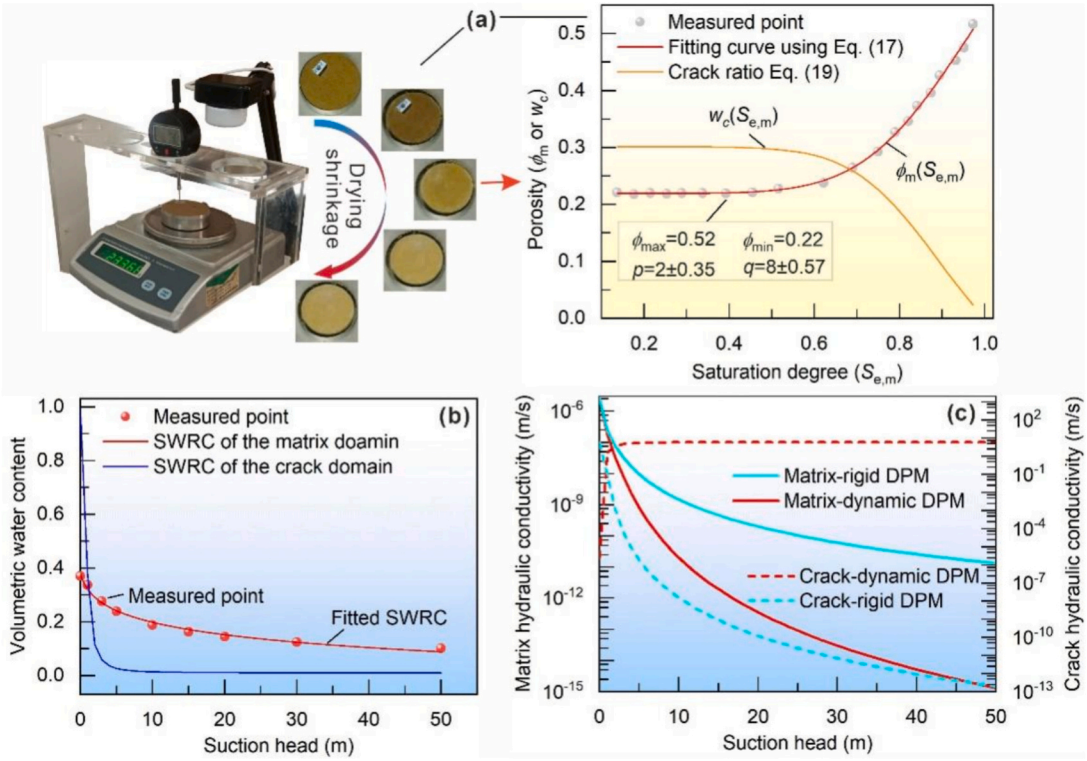

Fig. 7. Determination of soil shrink-swell parameters and hydraulic properties. (a) Laboratory shrinkage test and obtained shrinkage curve; (b) soil-water retention curve for the two models; (c) hydraulic conductivity functions for the two models.

atmospheric boundaries.

5.1. Hydro-mechanical slope stability model with dynamic DPM

Following Shao et al. (2015); (Shao et al., 2018), we adopted the local factor safety method (LFS) (Lu et al., 2012) to evaluate the slope stability. The local factor safety F_{LFS} is defined as the "ratio of the Coulomb stress at the current state of stress to the Coulomb stress of the potential failure state under the Mohr– Coulomb criterion". Then, application of the Mohr–Coulomb failure criterion gives the F_{LFS} at each node in the slope numerical model as follow

$$F_{LFS} = \frac{\tau^*}{\tau} = \frac{2\cos\phi'}{\sigma_1' - \sigma_3'}\left[c' + (\sigma_1' + \sigma_3')\tan\phi'/2\right] \quad (24)$$

$$\sigma' = \sigma - \chi p_w \quad (25)$$

where τ^* is the critical Coulomb shear strength; τ is the actual shear stress; c' is the effective cohesion (kPa); ϕ' is the effective friction angle; σ_1' and σ_3' are the spatially varying first and third principal effective stress, respectively. σ' is defined as normal stress (σ) minus pore water pressure (p_w); χ is the matric suction coefficient, which equals to the soil saturation degree (S_e). By substituting the pore water pressure and saturation degree simulated by the dynamic DPM into Eq. (25), a hydro-mechanically coupled slope stability model that accounts for desiccation crack dynamics can be established.

To describe the deterioration effect of desiccation cracks on soil strength parameters, we made the following two assumptions:

(i) The overall soil shear strength and corresponding strength parameters (c' and ϕ') are proportionally to the crack and matrix domains.

$$\tau = w_c\tau_c + w_m\tau_m \quad (26)$$

$$c' = w_c c_c' + w_m c_m' \quad (27)$$

$$\phi' = w_c\phi_c' + w_m\phi_m' \quad (28)$$

where τ_c is the soil shear strength. Note that the τ_c, c_c' and ϕ_c' are set as zero to describe the negative contribution of the crack domain on the overall soil strength.

(ii) The deterioration effect caused by desiccation cracks on the overall soil strength is unrecoverable when the cracks are closed due to rewetting. In other words, the overall strength parameters will decrease after soil cracking and will not recover after crack closure.

Fig. 11 illustrates the flowchart of coupling rigid DPM and dynamic DPM with the soil mechanical model. We specifically included the coupling process of a single-domain model (SDM) in the flowchart to better display the entire coupling process. As can be seen, for conventional SDM, the calculated pore water pressure is directly incorporated into the soil mechanical model using Eq. (25). For the rigid DPM and dynamic DPM, the pore water pressure used in Eq. (25) is a weighted value calculated from the matrix and crack domains (such as Eq. (5)). With regard to the matric suction coefficient, only the saturation degree of the matrix domain is considered, as the crack domain rarely contributes to overall soil strength through matric suction.

5.2. Design of numerical experiments

Dual-permeability and slope stability were also simulated and coupled within the finite element solver COMSOL Multiphysics 5.6 (Luo et al., 2023a; Shao et al., 2015). As shown in Fig. 12B, this study adopted a conceptual slope model with slope angle of 23°, which is 6 m high and 15 m long, consisting of a shrink-swell soil layer with 2.0 m thick and underlying low-permeable soil layer without cracks. The calculation

Table 1
The summary of hydrological parameters in rigid and dynamic dual-permeability models.

Symbol	Parameter description	Unit	Value		Source
			rigid DPM	dynamic DPM	
$\theta_{m,s}$	Matrix saturated volumetric moisture content	(−)	0.368		Measured
$\theta_{m,r}$	Matrix residual volumetric moisture content	(−)	0.01		Measured
α_m	van-Genuchten SWRC parameter (matrix	(1/m)	0.5	Eq. (22)	Measured
n_m	domain)	(−)	1.4		Measured
$K_{m,max}$	Matrix hydraulic conductivity maximum (pre-shrinkage)	(m/s)	2.62×10^{-6}		Measured
$\theta_{c,s}$	Crack saturated volumetric moisture content	(−)	0.99		Assigned
$\theta_{c,r}$	Crack residual volumetric moisture content	(−)	0.01		Assigned
α_c	van-Genuchten SWRC parameter (crack	(1/m)	1.5		Assigned
n_c	domain)	(−)	3		Assigned
$K_{c,max}$	Crack hydraulic conductivity maximum (maximum aperture)	(m/s)	5.9		Caculated
$K_{c,min}$	Crack hydraulic conductivity minimum (minimum aperture)	(m/s)	NA	2.62×10^{-6}	Assigned
K_a	Matrix-crack domain hydraulic conductivity	(m/s)	Eq. (8)		Caculated
a_w	Inter-domain water transfer coefficient	(1/m^2)	2564		Caculated
ϕ_{max}	Porosity maximum (matrix domain)	(−)	NA	0.52	Measured
ϕ_{min}	Porosity minimum (matrix domain)	(−)	NA	0.22	Measured
p	Shape parameters of the	(−)	NA	2	Measured
q	soil shrinkage curve	(−)	NA	8	Measured
w_c	Fixed crack proportion for the rigid DPM	(−)	0.3	NA NA	Measured

domain was set as 42 m by 25 m, which is wider than the slope model to minimize the boundary effects.

In hydrological simulations, the left and bottom sides of the model were defined as no-flux boundaries, while the right side encompasses a seepage boundary condition for the upper soil layer and a specified pressure head boundary for the lower soil layer. The upper surface boundaries were assigned a combined type of boundary conditions to represent rainfall, ponding, evaporation and seepage processes. In slope stability simulations, the left and right sides were designated as roller boundaries (allowing only vertical deformation), the bottom side was fixed (no deformation), and the upper surface was set as a free deformation boundary. A mesh structure with a dense size of 0.42 m was employed to capture transient boundary hydrological conditions. A coarser free-triangle mesh was used in the lower part of the model. The total number of mesh elements is 3565, with an average element area of 0.27 m^2. Numerical robustness was ensured through: (1) Mesh independence confirmed by sensitivity tests with average element sizes of 0.72 m^2 and 1.5 m^2; (2) Adaptive time-stepping with free step size control (initial $\Delta t = 0.001$ day); (3) Convergence criteria of relative tolerance 0.01 and absolute tolerance 1×10^{-5} kPa, with absolute tolerance factor fixed at 0.1 for pressure magnitude consistency. The initial condition for dynamic DPM and rigid DPM was obtained by running dynamic DPM under a rainfall intensity of 0.5 mm/day for a duration of 10 years to establish a stable initial distribution of pore water pressure (Fig. 12B). Then, the two models were subsequently subjected to one-year realistic atmospheric boundary conditions as illustrated in Fig. 12C following Luo et al. (2023b). The rigid DPM and dynamic DPM both utilize identical two-dimensional size, boundary conditions, mesh configurations and initial conditions.

In hydrological simulations, we compared the differences in groundwater level, water balance and pore water pressure distribution between dynamic DPM and rigid DPM. Then, building on the pore water pressure calculated by the two models, we compared the differences in slope stability among models under conditions of neglecting crack deterioration effect (dynamic DPM-1 and rigid DPM-1), considering reversible crack deterioration effect (dynamic DPM-2 and rigid DPM-2) and considering irreversible crack deterioration effect (dynamic DPM-3).

5.3. Parameterization

The implementation of the hydro-mechanical slope model requires both hydrological and mechanical parameters. The hydrological parameters all from Table 1. The mechanical parameters are primarily based on those outlined by Shao et al. (2015), with a slight modification: the soil shear strength parameters employed herein are higher compared to those in the referenced study to accommodate and observe the deteriorative effects on soil strength induced by long-term crack dynamics. Considering that the upper soil layer has undergone prolonged wetting-drying cycles and their soil strength may be degraded by the desiccation cracks, the lower layer was assigned with higher strength parameters than the upper one. Furthermore, it should be noted that elastic mechanical parameters were selected for this study, primarily due to the gentle slope inclination, which minimizes the likelihood of large and rapid plastic deformation (Zhang et al., 2021a). A summary of all mechanical parameters in each experiment is provided in Table 4.

6. Simulation results

6.1. Slope hydrology

6.1.1. Groundwater level and water balance

Our hydrological simulation results demonstrate that under atmospheric rainfall-evaporation conditions, desiccation cracks in the dynamic DPM overall lead to shallower groundwater level (Fig. 13A) and more water storage (Fig. 13C) compared to that of the rigid DPM with fixed cracks. This result seems to be counter-intuitive, but it becomes clear when we analyze the water balance of the boundary flow (Fig. 13B). Due to fixed cracks with larger preferred infiltration paths, the simulated cumulative preferential inflow and matrix inflow in the rigid DPM is 1.47 m^2 (10.6 %) higher than that of the dynamic DPM (Fig. 13b1-b2). However, as the fixed cracks concurrently result in high drainage capacity, the cumulative preferential outflow, near the slope toe and from the right boundary, is 17.6 m^2 higher than that of dynamic cracks (Fig. 13b5, b6, b11, b12). It means almost all up-boundary inflow in the rigid DPM is drained out through fixed preferential paths, and therefore, the dynamic DPM with decreasing crack connectivity retains more water in the slope (Fig. 13C). This phenomenon was also observed in the slope model test.

6.1.2. Pore water pressure and crack dynamics

The distribution of total pore water pressure further directly demonstrates the higher pore water pressure in the dynamic DPM with respect to the rigid DPM (Fig. 14). Particularly, during the heavy rainfall on the 197th day, dynamic DPM forms continuous wetting zones near the slope surface and at the two-layer interface, which connects to the groundwater around the slope toe. Conversely, the rigid DPM only forms small part of wetting zones around the slope toe. Following long-term drought (on the 280th day), the overall distribution of pore water pressure simulated in the desiccation cracks remains higher than that in the fixed cracks.

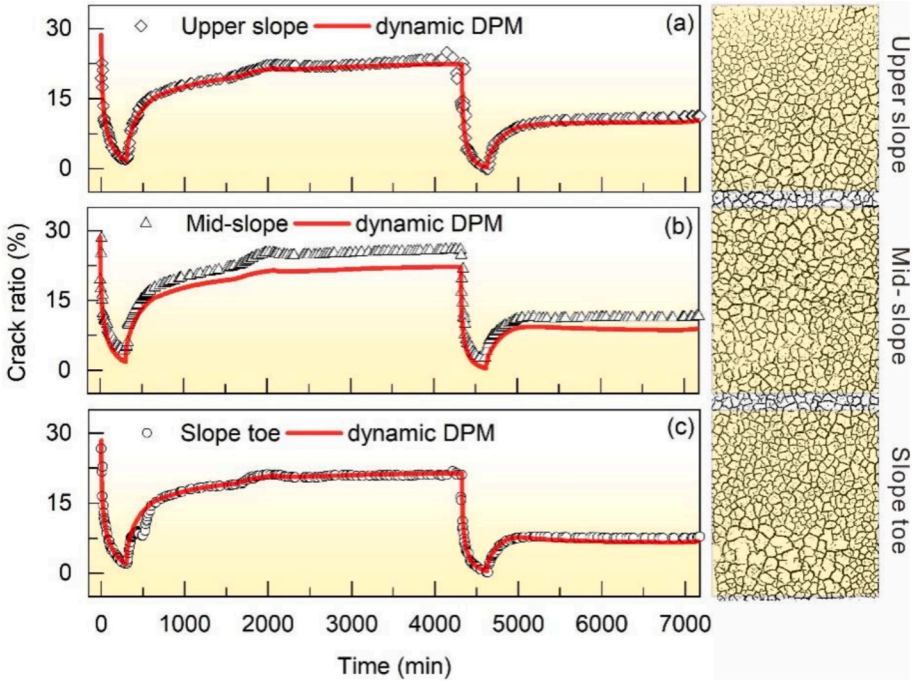

Fig. 8. Measured and simulated crack ratio in different positions.

Table 2
Statistical evaluation of prediction accuracy for crack ratio simulated by dynamic DPM.

Evaluation metrics	Upper slope	Mid-slope	Slope toe
RMSE	1.95	3.28	1.41
Nash-Sutcliffe efficiency (NSE)	0.92	0.81	0.96

The higher pore water pressure in the dynamic DPM is not only ascribed to its higher water storage but also comes from the desiccation crack dynamics. Fig. 15 A shows that the crack ratio (or crack proportion) in the dynamic DPM varies in time and space with the rainfall-evaporation cycles (Fig. 15a-a3), while the crack ratio in the rigid DPM is fixed at 10 % throughout the entire slope (Fig. 15a4). Especially during the heavy rainfall on the 197th day, due to matrix swelling induced by water infiltration, the average crack ratio simulated by the dynamic DPM is less than 1 %. Fig. 15 B shows pore water pressure in the crack domain and the water exchange rate during the 197th day (rainstorm). A positive water exchange rate indicates the movement of water from the crack domain to the matrix domain, whereas a negative value signifies the reverse flow. PWP represents pore water pressure. Under the same water inflow, crack domain in the dynamic DPM is rapidly filled due to shrinking water storage space, resulting in higher pore water pressure (Fig. 15b1) with respect to the rigid DPM (Fig. 15b2). The higher pore water pressure in the dynamic DPM contributes to faster water exchange from the crack domain (positive value) to the matrix domain (Fig. 15b3-b4) instead of being discharged through the right boundary, and therefore, forming larger wetting zones than that of the rigid DPM (Fig. 14).

6.2. Slope stability

The effective stress of the soil is defined as the total stress minus the pore water pressure (see Eq. (25)). Generally, regions with low effective stress in a slope are more prone to instability. Fig. 16A shows that the area of low effective stress simulated by the dynamic DPM is larger than that of the rigid DPM. Particularly on the 197th day, the average difference of effective stress between dynamic DPM and rigid DPM reaches −10 kPa. However, after prolonged drought (e.g., on the 364th day), this difference significantly decreases.

This outcome has direct implications for slope stability. For instance, when disregarding crack deterioration effects (Fig. 17a), dynamic DPM demonstrates substantially larger areas of slope instability ($F_s < 1$) and potential instability ($F_s < 1.2$) compared to the rigid DPM throughout the simulation period. It is consistent with the simulation result of effective stress distribution. Interestingly, when considering reversible crack deterioration effects, although areas with $F_s < 1$ and $F_s < 1.2$ during rainy season simulated by the dynamic DPM are still larger than those of the rigid DPM, areas with $F_s < 1.2$ during dry periods in the rigid DPM exceed those in the dynamic DPM (Fig. 17b). This outcome arises because, during drying periods, the difference in effective stress between the two models is minimal, making strength parameters the dominant factor influencing stability. In the rigid DPM, the fixed crack proportion ($w_c = 0.1$) results in an average 10 % reduction in soil strength throughout the simulation, whereas the maximum average reduction predicted by the dynamic DPM is only 3.8 %. Furthermore, when considering irreversible crack deterioration effects (dynamic DPM-3 in Fig. 17c), the areas of $F_s < 1$ and $F_s < 1.2$ are largest in dynamic DPM-3, followed by those in dynamic DPM-2 (considering reversible crack deterioration effects) and dynamic DPM-1 (neglecting crack deterioration effects). This result is not surprising when examining changes in strength parameters (e.g., cohesion). As shown in Fig. 18, in dynamic DPM-3, even as the crack ratio decreases during rainfall, the irreversible crack deterioration effect maintains overall soil cohesion at levels reduced by the maximum previous crack ratio. In contrast, due to crack closure during rainfall, the assumption of reversible crack deterioration in dynamic DPM-2 results in soil strength similar to its initial strength, without significant reduction. Consequently, the areas of $F_s < 1$ and $F_s < 1.2$ in dynamic DPM-2 largely overlap with those in dynamic DPM-1.

7. Discussion

7.1. Effects of desiccation crack dynamics on slope hydrology

Our study highlights the important role of the opening and closing process of desiccation cracks for slope hydrology and impacting the

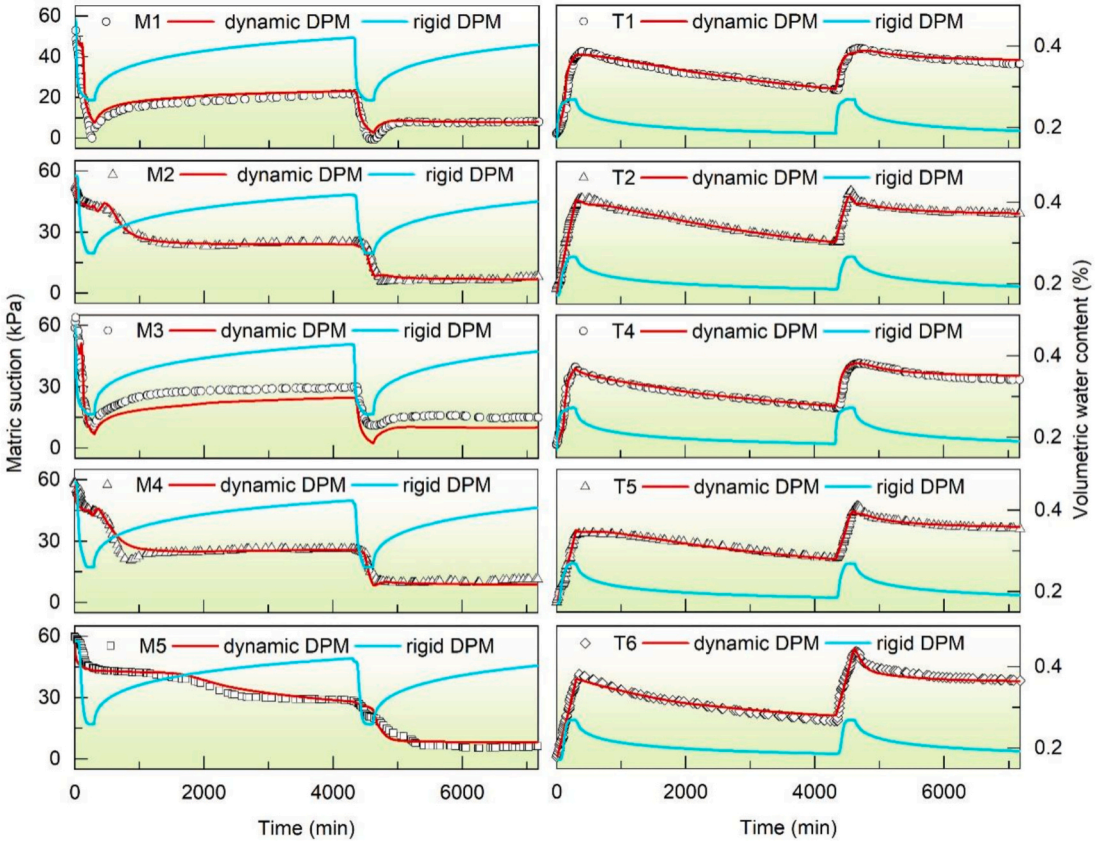

Fig. 9. Measured and simulated matric suction (left graphs) and volumetric water content (right graphs) in different positions.

Table 3
Statistical evaluation of prediction accuracy for matric suction and water content simulated by DPMs.

Evaluation metrics	Dynamic DPM					Rigid DPM				
	M1	M2	M3	M4	M5	M1	M2	M3	M4	M5
RMSE	4.59	1.45	4.71	2.29	3.02	17.09	15.54	14.49	16.80	16.16
Nash-Sutcliffe efficiency (NSE)	0.87	0.98	0.92	0.98	0.98	−0.75	0.41	0.28	0.31	0.51
Evaluation metrics	T1	T2	T4	T5	T6	T1	T2	T4	T5	T6
RMSE	0.027	0.025	0.045	0.042	0.048	0.11	0.12	0.10	0.11	0.12
Nash-Sutcliffe efficiency (NSE)	0.96	0.97	0.88	0.89	0.88	0.41	0.32	0.39	0.35	0.29

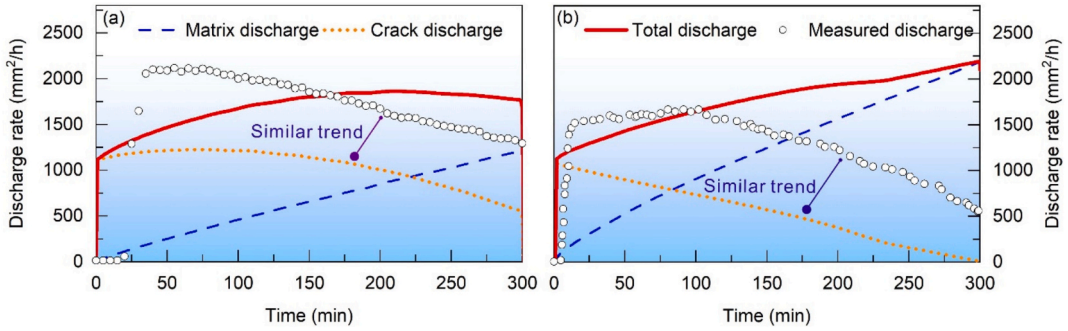

Fig. 10. Measured and simulated slope discharge by dynamic DPM. (a) discharge during the 1st rainfall (b) discharge during the 2nd rainfall

stability of expansive clay slopes. Previous studies have identified the preferential flow through desiccation cracks is the leading hydrological cause for expansive clay slope instability (Bogaard and Greco, 2015; Caris and Van Asch, 1991; Greco et al., 2023; Khan et al., 2017; Luo et al., 2021; Pei et al., 2020; Xie et al., 2020; Zhang et al., 2022a; Zhang et al., 2021b; Zhang et al., 2021a; Zhang et al., 2020). Zhang et al. (2021b); (Zhang et al., 2021a) found early responses of deep soils to precipitation induced by preferential flow through desiccation cracks, attributed to sharp increase of pore water pressure which facilitates expansive clay slope instability. Pei et al. (2020) and Xie et al. (2020) underscores that preferential flow through desiccation cracks reduces surface runoff and increases infiltration, leading to reduced stability of

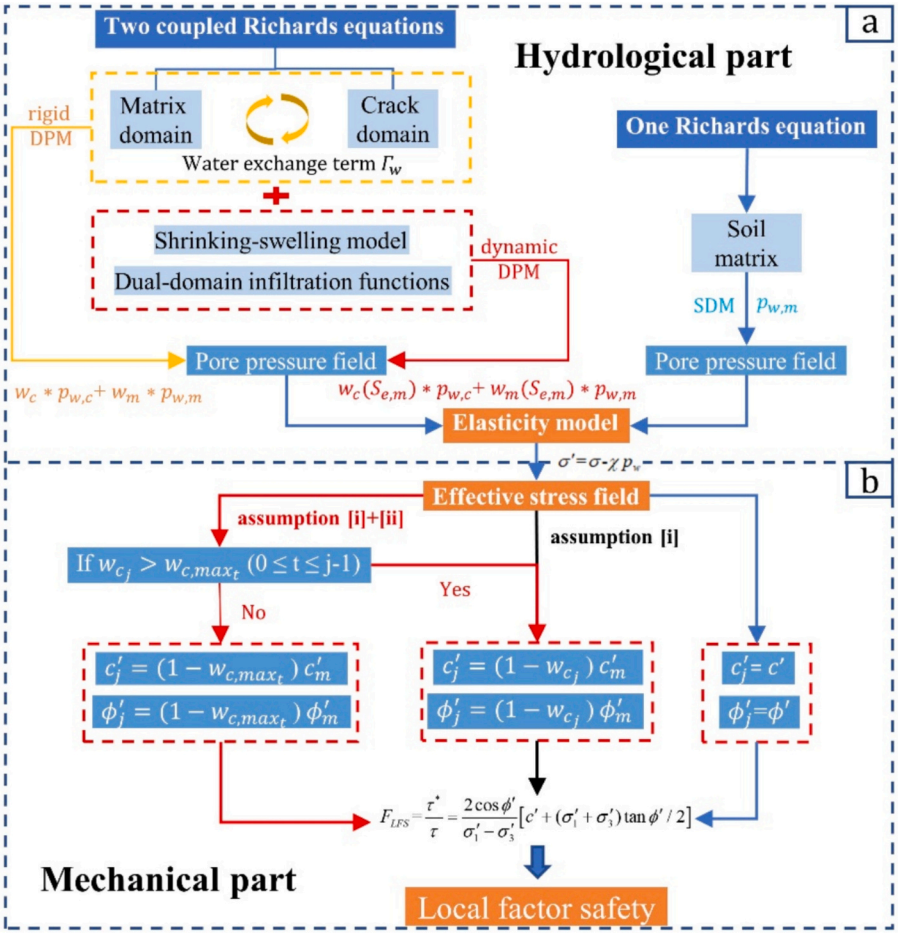

Fig. 11. Flow chart of coupling SDM, rigid DPM and dynamic DPM to slope stability mechanical model. (a) Hydrological part; (b) Mechanical part involving dual-strength assumptions. Note that 'Two coupled Richards equations' represents rigid DPM and dynamic DPM, while 'One Richards equation' represents SDM.

expansive clay slopes. Most existing studies have focused on the negative effects of preferential flow during crack opening, assuming that the closure of desiccation cracks reduces preferential flow and thus enhances slope stability. However, in this paper, we delineate, for the first time, that narrowing of desiccation cracks could slow down the lateral slope drainage process during high-intensity precipitations due to reduced connectivity in the crack network. This, in turn, leads to rapid increase in pore water pressure and water exchange from the crack domain to soil matrix, ultimately contributing to slope instability. Galeandro et al. (2013a); (Galeandro et al., 2013b) conducted simulations of preferential flow through vertical shrinkage cracks and obtained similar results, with overland flow quickly reaching significant depths through narrowing cracks and increasing pore water pressure. However, in their case, the high pore pressure in the narrowing cracks broke a capillary barrier formed by an underlying high-permeable soil layer, promoting vertical water drainage and benefiting slope stability. In contrast, our study focused on another and also more common slope structure, featuring a combination of an expansive clay layer and a low-permeable soil layer below. In this scenario, the vertical drainage paths established by desiccation cracks are constrained by a low-permeable soil layer beneath, forcing drainage to occur laterally through the desiccation cracks. As the crack apertures narrow, the connectivity of these lateral paths decreases, leading to increased pore water pressure and ultimately triggering slope instability. Our findings suggest that, instead of arbitrarily closing desiccation cracks, maintaining an appropriate level of crack connectivity may offer a more nature-based and effective approach to prevent slope failures in expansive clays. For instance, implementing controlled-connectivity strategies—such as bioengineered root channels or graded gravel trenches—can sustain lateral drainage capacity during crack closure, thereby enhancing the climate resilience of cracked expansive clay slopes. Nevertheless, it is worth noting that our results are mainly applicable and interpretable to gently sloping expansive clay slopes where desiccation cracks can well develop instead of being eroded by surface runoff. Additionally, beyond conventional monitoring of surface crack propagation during droughts, we recommend prioritizing real-time tracking of crack-network connectivity during storms.

7.2. *Effects of desiccation crack dynamics on slope mechanical stability*

Our study also reveals that irreversible deterioration effect caused by dynamic changes of desiccation cracks can persistently degrade long-term slope stability. Mechanistically, clay slope instability arises from two interdependent processes: (1) progressive decline in suction-dependent shear strength driven by moisture content variations (Lade, 2010; Toll et al., 2011; Wu et al., 2022; Zhan et al., 2013), and (2) time-dependent weakening of inherent strength characteristics (e.g. cohesion and friction angle) governed by structure evolution (Smethurst et al., 2012; Stirling et al., 2021; Take and Bolton, 2011; Zhang et al., 2022b; Zhou et al., 2021; Tian et al., 2025; Huang et al., 2020). During drying periods, the strength of soil matrix increases as soil suction rises. Concurrently, drying of the soil leads to development of desiccation cracks, resulting in reduction of overall shear strength. There is a competitive relationship between the contribution of increasing soil matrix strength to the overall strength and the reduction in the overall strength caused by cracks (Tang et al., 2020). During subsequent wetting

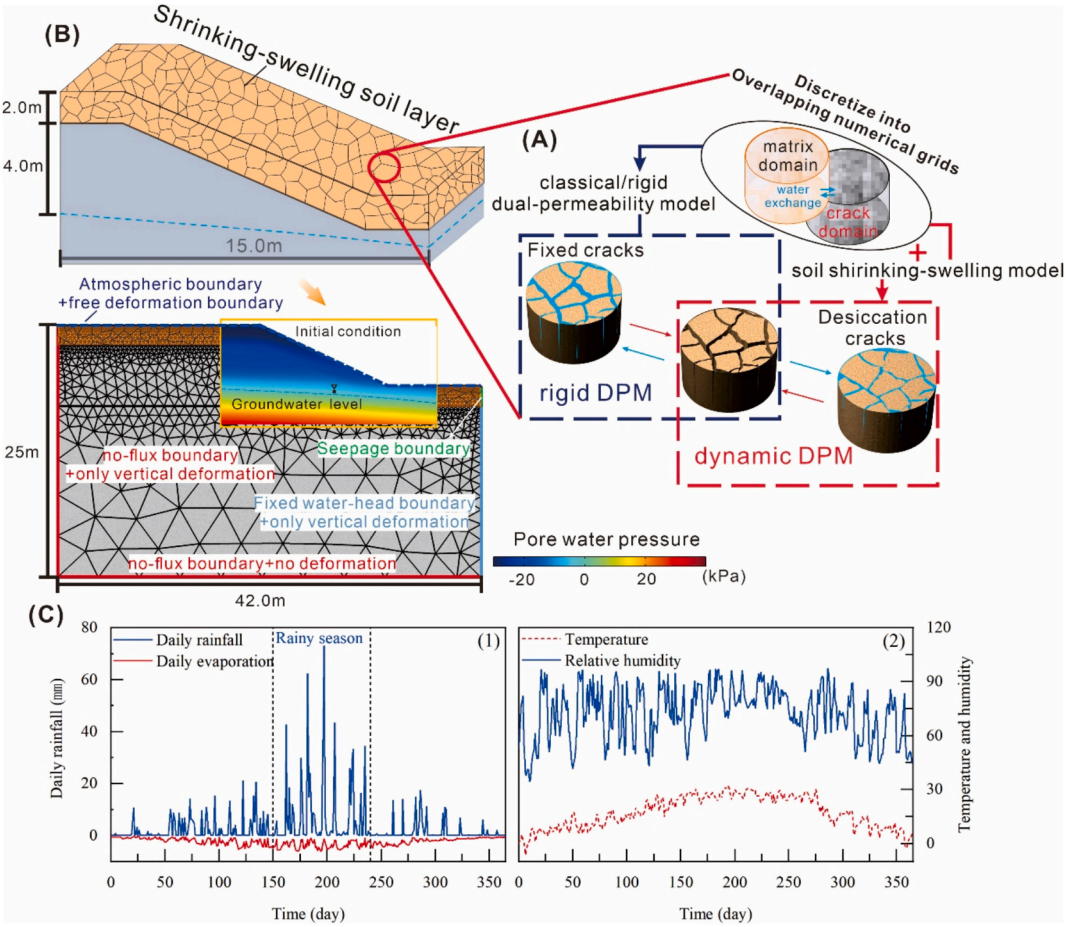

Fig. 12. Simulation set-up of slope hydrology and stability using rigid and dynamic DPM. (A) schematic of rigid DPM assuming fixed cracks and dynamic DPM considering varying desiccation cracks; (B) schematic of the conceptual expansive clay slope model and its 2-D numerical forms involving the boundary conditions, mesh structure and initial conditions; (C) one-year atmospheric boundary conditions.

Table 4
Mechanical parameters for all models.

Model	Symbol	Parameter description		Unit	Upper layer	Lower layer
dynamic DPM-1 rigid DPM-1	E	**Neglecting** deterioration effect of desiccation cracks on soil strength	Young's modulus	(MPa)	10	20
	ν		Poisson's ratio	(–)	0.35	0.35
	ϕ'_m		Friction angle	(°)	10	35
	c'_m		Effective cohesion	(kPa)	8	15
	γ		Natural unit weight	kN/m^3	1900	2100
dynamic DPM-2	ϕ'_m	Considering **reversible** deterioration effect of desiccation cracks on soil strength	Friction angle **(assumption [i])**	(°)	$10*(1-w_c(S_{e,m}))$	35
	c'_m		Effective cohesion **(assumption [i])**	(kPa)	$8*(1-w_c(S_{e,m}))$	15
rigid DPM-2	ϕ'_m		Friction angle **(assumption [i])**	(°)	$10*(1-w_c)$ =10.8	35
	c'_m		Effective cohesion **(assumption [i])**	(kPa)	$8*(1-w_c)$ =7.2	15
dynamic DPM-3	ϕ'_m	Considering **irreversible** deterioration effect of desiccation cracks on soil strength	Friction angle **(assumption [i] + [ii])**	(°)	$10*(1-w_c(S_{e,m}))$	35
	c'_m		Effective cohesion **(assumption [i] + [ii])**	(kPa)	$8*(1-w_c(S_{e,m}))$	15

periods, the strength of soil matrix decreases as soil suction lowers. Meanwhile, wetting of the soil leads to narrowing of desiccation cracks. The soil suction-derived shear strength fluctuates with moisture dynamics and is reversible during wetting and drying. However, intrinsic soil structure is vulnerable to damage from the opening and closing processes of desiccation cracks, leading to an irreversible decline in strength parameters (Pires et al., 2020; Tang et al., 2020; Xu et al., 2021). Earlier numerical studies have considered soil suction-derived shear strength but often assumed constant soil strength parameters, thus failing to capture the continuous degradation of slope stability under wetting-drying cycles. Gao et al. (2021) introduced a reduction function to characterize soil strength with wetting-drying cycles, but their approach is highly empirical and does not account for the irreversible deterioration caused by desiccation cracks. In our study, we

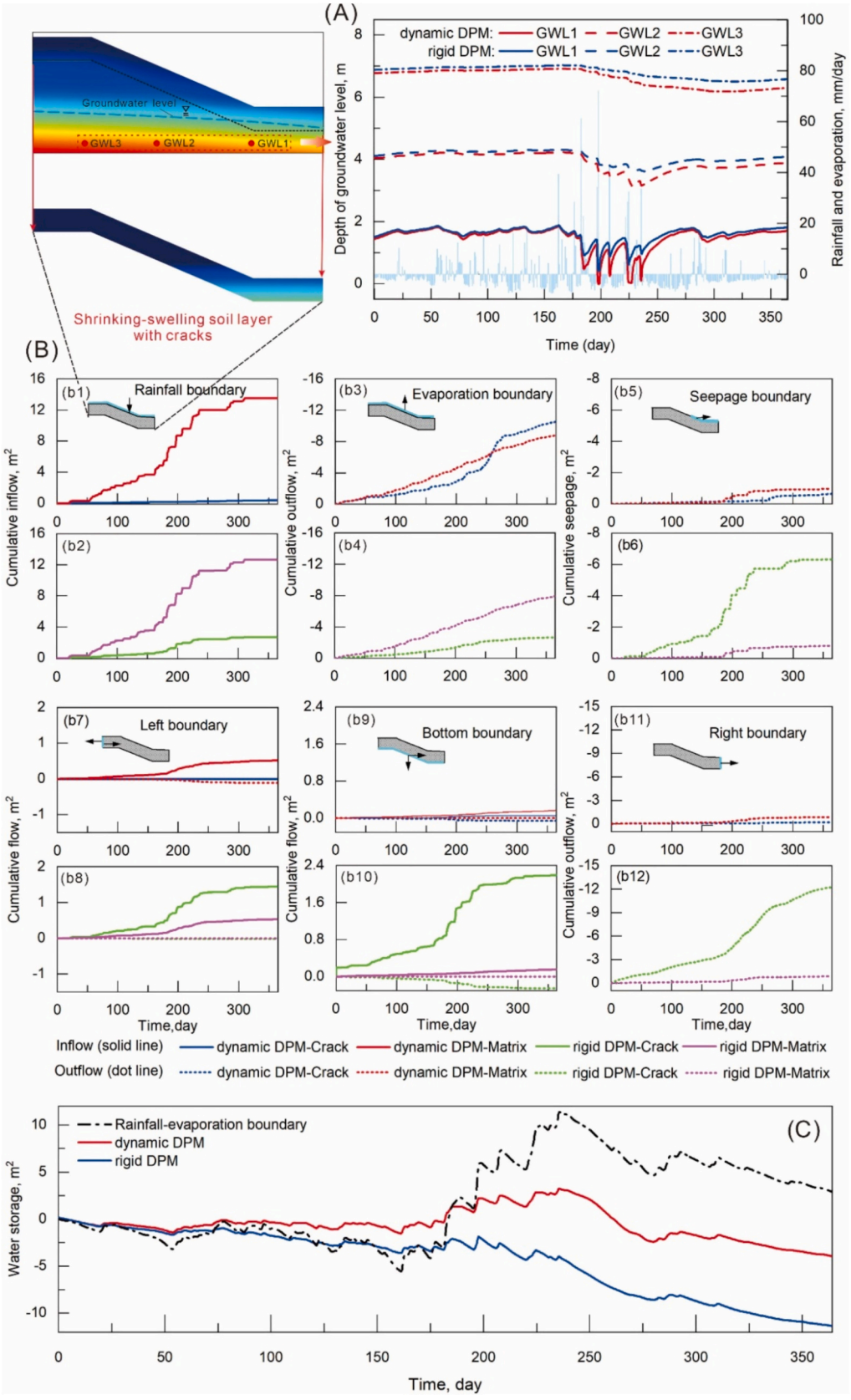

Fig. 13. Groundwater level and water balance simulated by the rigid DPM and dynamic DPM. (A) variation of depth of groundwater level at three different monitoring point simulated by the two models; (B) boundary water inflow and outflow in the upper expansive clay layer; (C) time curves of cumulative water storage in the expansive clay layer simulated by the rigid DPM and dynamic DPM. Note that the cumulative water storage equals to the difference between water inflow and outflow.

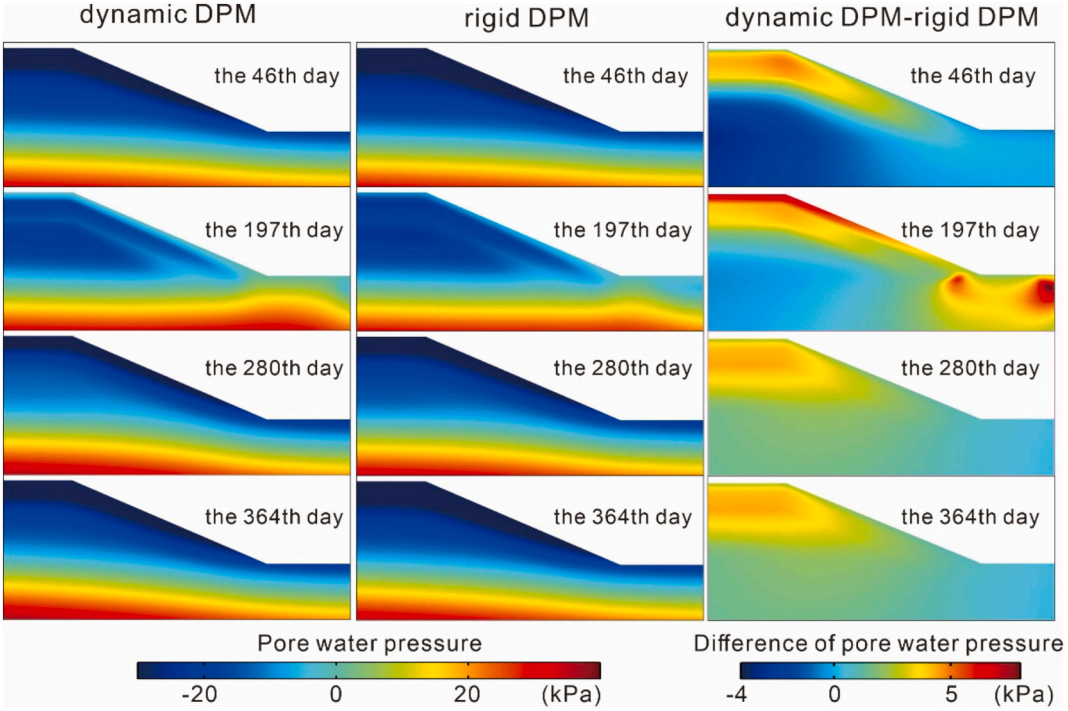

Fig. 14. Distribution of pore water pressure simulated by the two models and their differences.

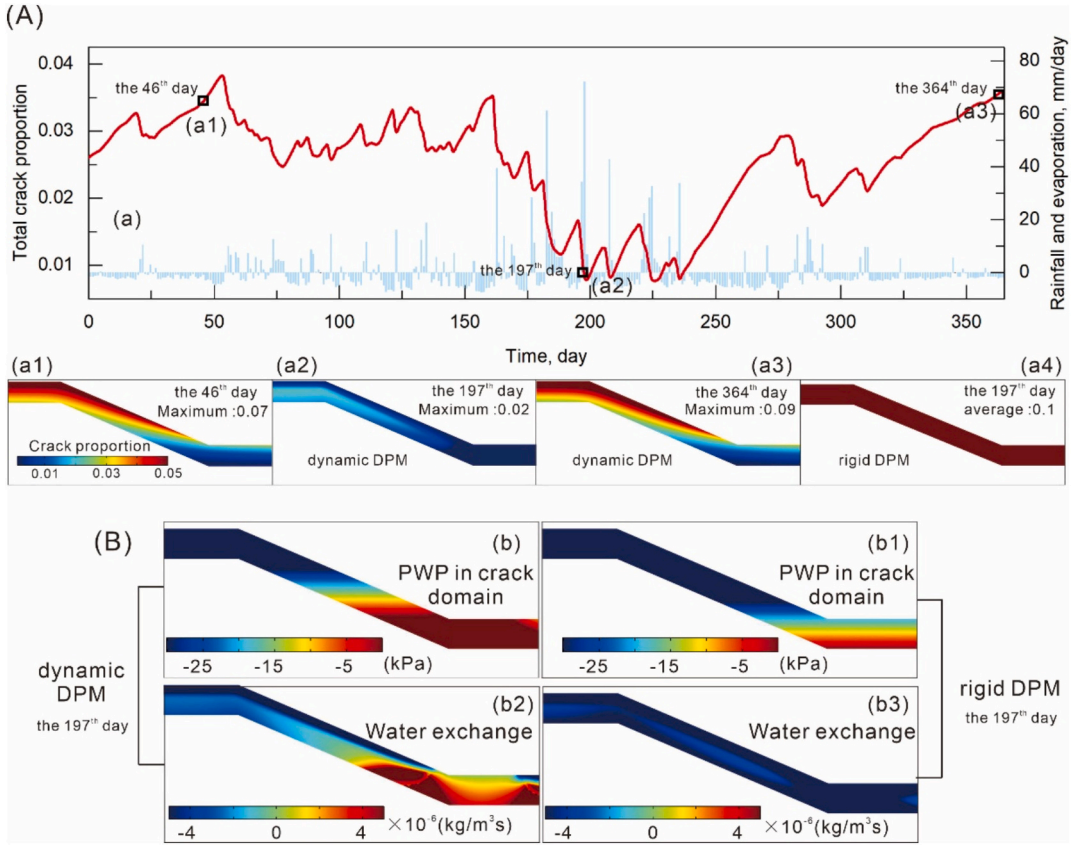

Fig. 15. Desiccation crack dynamics and water exchange simulated by the rigid DPM and dynamic DPM. (A) spatiotemporal variation of total crack proportion in the two models; (B) pore water pressure in the crack domain and the water exchange rate during the 197th day (rainstorm).

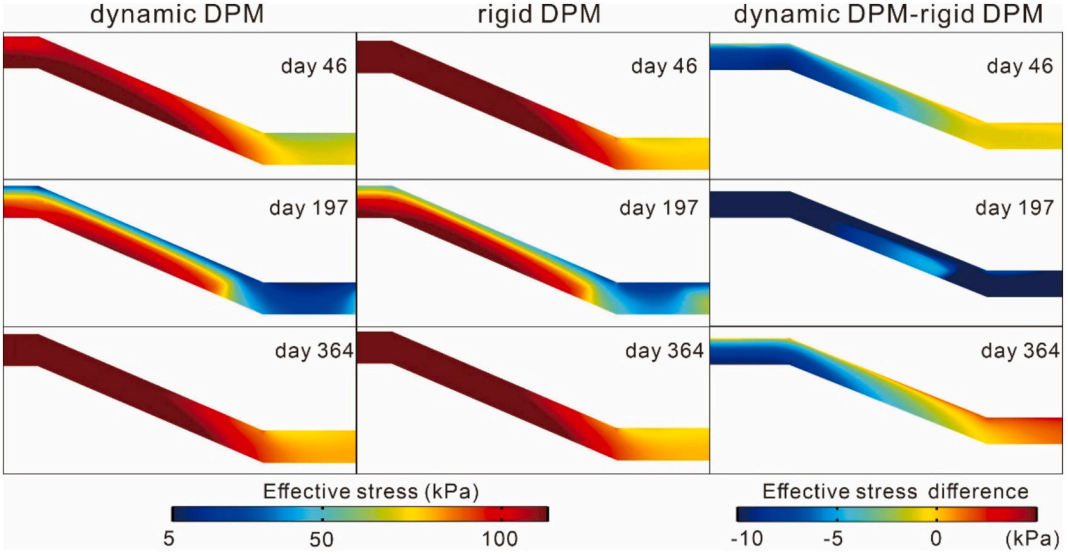

Fig. 16. Distribution and differences of effective stress simulated by rigid DPM and dynamic DPM.

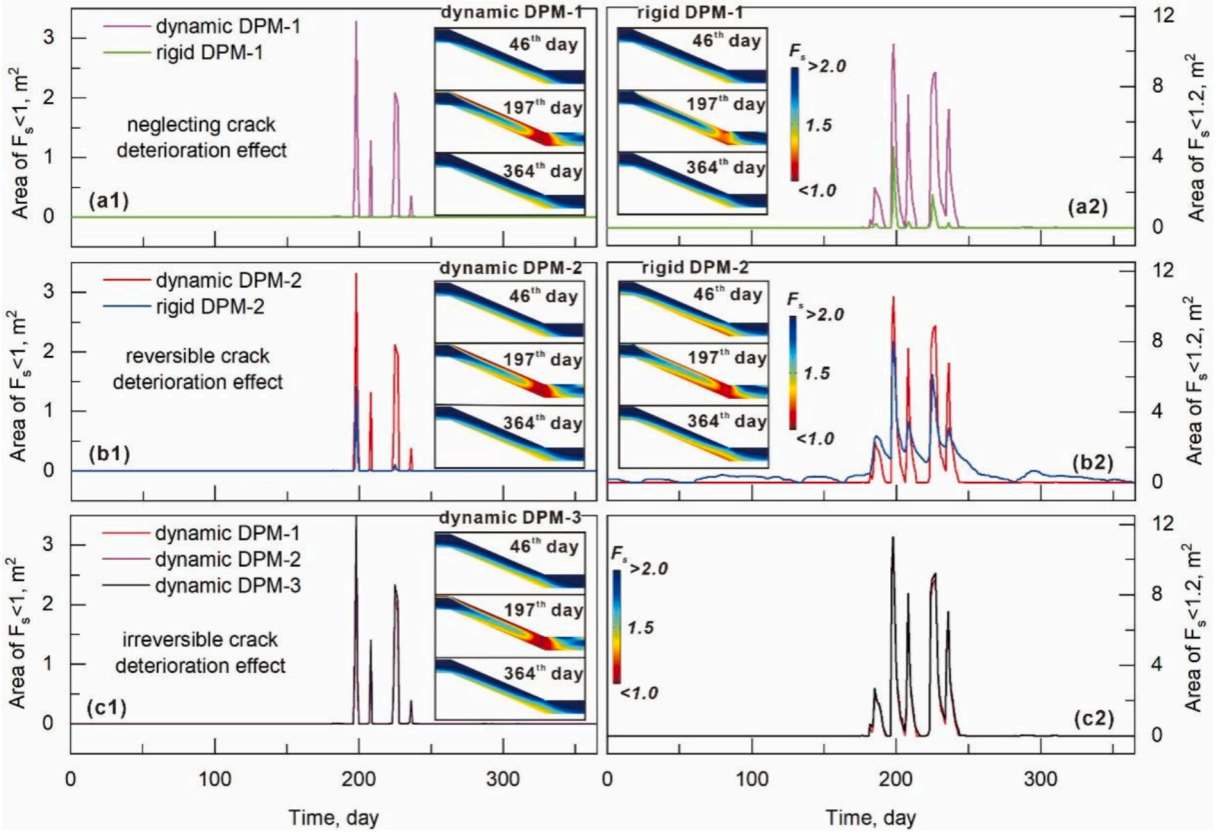

Fig. 17. Area of slope instability (Fs < 1) and potential instability (Fs < 1.2) and their cloud graphs in the case neglecting crack deterioration effect (dynamic DPM-1, rigid DPM-1), considering reversible crack deterioration effect (dynamic DPM-2, rigid DPM-2) and considering irreversible crack deterioration effect (dynamic DPM-3) on the soil strength.

quantify the deterioration of soil strength parameters as a function of crack proportion and employ a linear irreversible reduction method to demonstrate that the development of desiccation cracks leads to irreversible damage to the intrinsic strength parameters of soil, even when the cracks heal. Although the difference in slope failure areas is only 1.2 % between simulations considering irreversible crack deterioration effects and not, it is foreseeable that extended periods of drought will increase crack volume and lead to further soil strength deterioration, significantly elevating the risk of slope instability during subsequent rainy seasons. It might provide plausible interpretations for weather-driven deterioration effects on soil dams (Stirling et al., 2021). For slope stability assessments in climate-sensitive cracked clays, our results demonstrate that analyses must account not only for instantaneous crack-density effects but also dynamic strength attenuation from

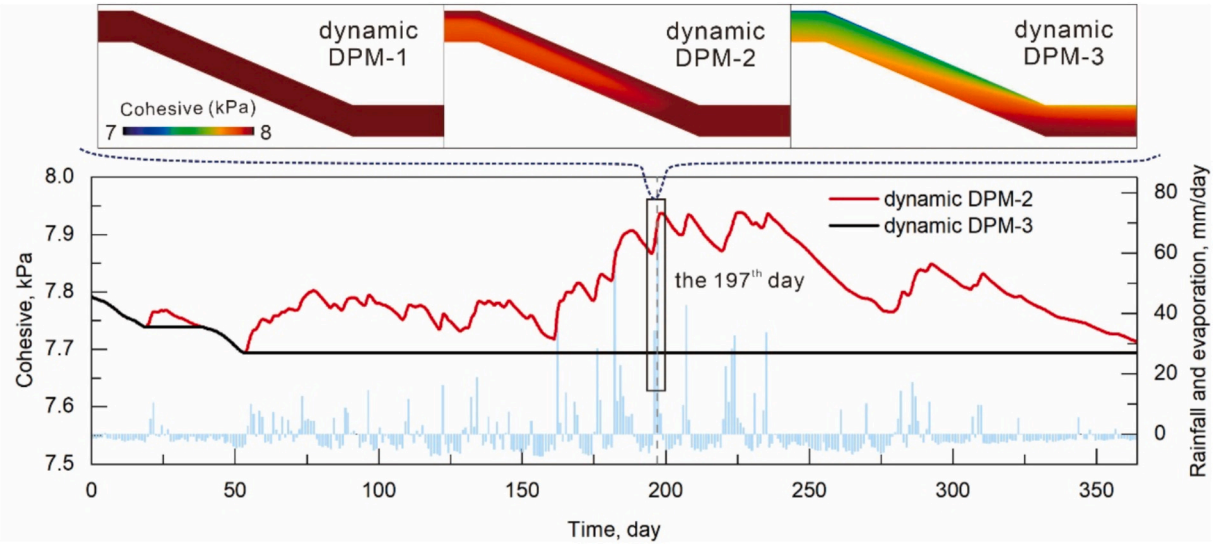

Fig. 18. Variation of average soil cohesive under considering reversible (dynamic DPM-2) and irreversible crack deterioration effect (dynamic DPM-3).

crack evolution.

7.3. Pore water pressures and slope stability

Within the dual-permeability framework, another issue meriting focused discussion is which pore water pressure (PWP) should be employed in the analysis of slope stability, that of the matrix domain or the crack domain. In previous studies involving the rigid DPM and slope stability in Shao et al. (2015, 2017, 2018), PWP in the crack domain has often been considered as the primary and sole variable in slope stability simulations. This may hold true for slopes composed of gravel soils with pervasive and high-density fixed macropores (Hencher, 2010; Laine-Kaulio et al., 2014; Nieber and Sidle, 2010; Uchida et al., 2001; Wienhöfer et al., 2011), where the time delay for PWP propagating from the crack domain to the matrix domain (or PWP equilibrium process) is very short (Shao et al., 2015). It implies that the PWP in the two domains can be close to each other in a short time, and therefore, it is reasonable to choose the PWP as the global PWP representation in slope stability calculation from a relatively safe perspective. However, it is not the case for cracked clay soil slopes, in which the time delay of PWP equilibrium process is relatively large (van der Spek et al., 2013). As shown in Fig. 19, in different locations of cracked clay slopes, the slow water balance process between the two domains leads to considerable differences in PWP at a given time. For the shallow surface layer (Fig. 19a), where the crack domain serves as the main drainage pathway, the difference between the PWP in the crack domain and that in the matrix

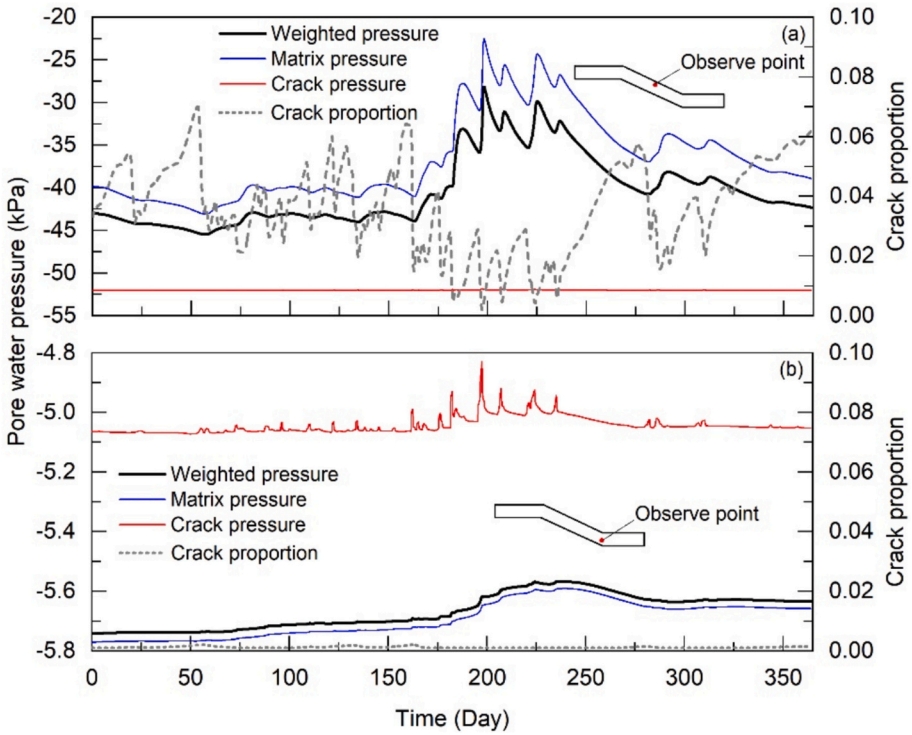

Fig. 19. Comparison graph of weighted and non-weighted pore water pressure at different slope position simulated by the dynamic DPM (a) surface layer at the mid-slope (b) 1-m depth at the slope toe.

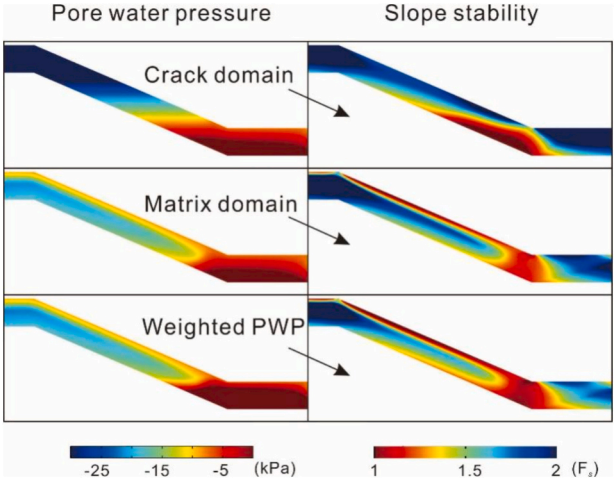

Fig. 20. Slope stability calculation based on different choice of pore water pressure simulated in dynamic DPM during the 197th day.

domain can reach up to approximately 25 kPa. Using crack PWP as the global PWP representation, as shown in Fig. 20, neglects the contribution of the matrix domain to slope instability and consequently underestimates the extent of unstable regions. For the slope toe (Fig. 19b), the crack domain acts as the primary water storage space and exhibits higher PWP values than the matrix domain, but its volume proportion is significantly smaller compared to the matrix domain. Using crack PWP as the sole variable to calculate the slope stability may lead to underestimation. Consequently, herein, we adopted weighted PWP of matrix and crack domains, instead of sole crack PWP, as the stress input for the slope stability simulation.

8. Conclusions

This study investigates the impact of desiccation crack dynamics on slope hydrology and stability in expansive clay slopes. An advanced hydrological model, capable of capturing both desiccation crack evolution and associated slope hydrological processes, was developed based on a dynamic dual-permeability model (dynamic DPM). The model was validated through small-scale physical slope experiments and subsequently integrated into numerical slope stability analyses under one-year atmospheric conditions. Using a synthetic slope model, the slope hydrological response was simulated under both dynamic and fixed crack conditions. The resulting hydrological outputs were then used to evaluate slope stability under three scenarios: (i) neglecting the deterioration effect of cracks on soil strength, (ii) considering reversible deterioration, and (iii) considering irreversible deterioration.

Regarding slope hydrology, the simulation results of dynamic DPM revealed that the slope model with dynamic cracks retained more water and higher groundwater level than that with fixed cracks. The closure process of desiccation cracks reduces slope drainage capacity, leading to a rapid build-up of pore water pressure due to preferential flow, and thus facilitating slope instability, which is a newfound and somewhat counter-intuitive triggering mechanism. Conversely, rigid DPM, which neglects the desiccation crack dynamics, significantly overestimates the water storage and drainage capacity of the crack domain, thus underestimating the overall pore water pressure in the slope. From the mechanical perspective, the irreversible deterioration effect induced by crack dynamics on soil strength persistently degrades long-term slope stability. Disregarding these deterioration effect will overestimate the slope stability in the context of climate change.

While the dynamic DPM advances crack-mediated hydrological modeling, three key limitations warrant attention. Firstly, the model validation relied on laboratory-scale slopes, necessitating further testing under field-scale heterogeneous subsurface conditions to ensure broader applicability. Secondly, although the implicit approach effectively quantifies crack-volume dynamics, it simplifies crack geometry by resolving neither individual propagation paths nor localized stress concentrations, potentially underestimating failure risks at fracture tips. Most critically, the current framework initiates simulations from pre-desiccated cracks, lacking capability to simulate the complete spatio-temporal evolution from intact soil to crack stabilization; future iterations will incorporate tensile strain thresholds and energy-based initiation criteria to enhance evolutionary completeness.

Notation

θ	Total water content (combined matrix and crack domains), m^3m^{-3}
θ_m	Volumetric water content of the matrix domain, m^3m^{-3}
θ_c	Volumetric water content of the crack domain, m^3m^{-3}
$\theta_{m,s}$	Saturated volumetric water content of the matrix domain, m^3m^{-3}
$\theta_{m,r}$	Residual volumetric water content of the matrix domain, m^3m^{-3}
$\theta_{c,s}$	Saturated volumetric water content of the crack domain, m^3m^{-3}
$\theta_{c,r}$	Residual volumetric water content of the crack domain, m^3m^{-3}
$S_{e,m}$	Saturation degree of the matrix domain, m^3m^{-3}
$S_{e,c}$	Saturation degree of the crack domain, m^3m^{-3}
α_m	Parameter for the van Genuchten water retention curve of the matrix domain, 1/m
n_m	Parameter for the van Genuchten water retention curve of the matrix domain, 1/m
α_c	Parameter for the van Genuchten water retention curve of the crack domain, 1/m
n_c	Parameter for the van Genuchten water retention curve of the crack domain, 1/m
h_m	Pressure head of the matrix domain, m
h_c	Pressure head of the crack domain, m
C_c	Specific water capacity of the crack domain which is defined as $d\theta_c/dh_c$, 1/m
C_m	Specific water capacity of the matrix domain which is defined as $d\theta_m/dh_m$, 1/m
K_s	Total transient saturated hydraulic conductivity of the soil (combined matrix and crack domains), m/s
K_c	Transient hydraulic conductivity of the crack domain, m/s
$K_{c,s}$	Saturated hydraulic conductivity of the crack domain, m/s
$K_{c,\max}$	The maximum crack hydraulic conductivity when the crack reaches its maximum crack aperture, m/s
$K_{c,\min}$	The minimum crack hydraulic conductivity when the crack reaches its minimum crack aperture, m/s
K_m	Transient hydraulic conductivity of the matrix domain, m/s
$K_{m,s}$	Saturated hydraulic conductivity of the matrix domain, m/s
$K_{m,\max}$	The maximum matrix hydraulic conductivity prior to soil shrinkage, m/s
K_a	Hydraulic conductivity between the matrix and crack domains, m/s
$K_{a_{\min}}$	An improved hydraulic conductivity between the matrix and crack domains reformulated by Gerke et al. (2013), m/s
Γ_w	Water exchange term between the crack and matrix domains, 1/s
w_c	Crack ratio, which is defined as volumetric ratio between the crack domain and the overall soil volume, m^3m^{-3}
$w_{j,\max}$	The maximum average crack aperture measured in the experiment, m
w_m	Volumetric ratio between the matrix domain and the overall soil volume, m^3m^{-3}
α_w	Effective water transfer coefficient, $1/m^2$

β	A dimensionless factor which depends on the shape of the soil matrix and is set as 3
γ_w	A dimensionless "scaling" coefficient with a suggested value of 0.4
a	A scaling factor approximately equaling to the half width of the average block size
i	Total boundary flow rate (combined matrix and crack domains), m/s
i_m	Transient boundary flow rate of the matrix domain, m/s
i_c	Transient boundary flow rate of the crack domain, m/s
r	Rainfall intensity, m/s
AE	Actual evaporation rate, m/s
PE	Potential evaporation rate, m/s
S	Matric suction of the soil surface, kPa
ϕ_{max}	The maximum porosity) of a soil core prior to soil shrinkage. m^3m^{-3}
ϕ_{min}	The minimum porosity of the matrix domain, m^3m^{-3}
ϕ_{matrix}	Porosity of the matrix domain, which is defined as pore volume in matrix divided by the total soil volume, m^3m^{-3}
ϕ_{crack}	Porosity of the crack domain, which is defined as pore volume in crack domain divided by the total soil volume, m^3m^{-3}
p	Functional shape parameters of the soil shrinkage curve
q	Functional shape parameters of the soil shrinkage curve
τ^*	Critical Coulomb shear strength, kPa
τ	Shear stress, kPa
c'	Effective cohesion, kPa
ϕ'	Effective friction angle, °
σ'	Effective stress, kPa
p_w	Pore water pressure, kPa
χ	Matric suction coefficient
E	Young's modulus, MPa
ν	Poisson's ratio

CRediT authorship contribution statement

Yi Luo: Writing – original draft, Validation, Software, Methodology, Conceptualization. **Jiaming Zhang:** Writing – review & editing, Supervision. **Chao-Sheng Tang:** Writing – review & editing, Conceptualization. **Guosheng Jiang:** Writing – review & editing, Supervision. **Thom Bogaard:** Writing – review & editing, Methodology, Conceptualization.

Declaration of competing interest

The authors declare that they have no known competing financial interests or personal relationships that could have appeared to influence the work reported in this paper.

Acknowledgments

This work was financially supported by the National Natural Science Foundation of China (Grant No. 42407204, 42177166, 42525201, 42230710), Postdoctoral Fellowship Program of CPSF (Grant No. GZC20232473), China Postdoctoral Science Foundation Funded Project (Grant No. 2024M763062) and Hubei Postdoctoral Innovation Talent Support Project (Grant No. 2024HBBHCXA088). It was also supported by the Fundamental Research Founds for National University, China University of Geosciences (Wuhan) and the Plan of Anhui Province Transport Technology Progress (Grant No. 2018030).

Data availability

Data will be made available on request.

References

Aguilar-López, J.P., Bogaard, T.A., Gerke, H.H., 2020. Dual-permeability model improvements for representation of preferential flow in fractured clays. Water Resour. Res. 56. https://doi.org/10.1029/2020wr027304.

Altay, U., Dorduncu, M., Kadioglu, S., Madenci, E., 2024. Bond-based peridynamic fatigue analysis of ductile materials with Neuber's plasticity correction. Eng. Comput. 41, 1771–1790. https://doi.org/10.1007/s00366-024-02092-x.

Beven, K., Germann, P., 1982. Macropores and water flow in soils. Water Resour. Res. 18, 1311–1325. https://doi.org/10.1029/WR018i005p01311.

Bogaard, T.A., Greco, R., 2015. Landslide hydrology: from hydrology to pore pressure. WIREs Water 3, 439–459. https://doi.org/10.1002/wat2.1126.

Bradley, C., Mosugu, M., Gerrard, J., 2007. Seasonal dynamics of soil–water pressure in a cracking clay soil. Catena 69, 253–263. https://doi.org/10.1016/j.catena.2006.06.004.

Caris, J.P.T., Van Asch, T.W.J., 1991. Geophysical, geotechnical and hydrological investigations of a small landslide in the French Alps. Eng. Geol. 31, 249–276. https://doi.org/10.1016/0013-7952(1)90011-9.

Chaduvula, U., Viswanadham, B.V.S., Kodikara, J., 2022. Centrifuge model studies on desiccation cracking behaviour of fiber-reinforced expansive clay. Geotext. Geomembr. 50, 480–497. https://doi.org/10.1016/j.geotexmem.2022.02.001.

Chen, X.-Y., Tang, C.-S., Cheng, Q., Zeng, Z.-J., Shi, B., 2024. Analysis of the stability of cracked soil slopes using a numerical model incorporating stochastic theory. Comput. Geotech. 167. https://doi.org/10.1016/j.compgeo.2024.106067.

Chen, X.Y., Tang, C.S., Luo, Y., Vahedifard, F., Tian, B.G., Wang, T., Zeng, Z.J., Cheng, Q., 2025. Exploring the hysteresis effects of climate-induced desiccation cracks on slope stability: new insights from experimental and numerical studies. Case Rep. Med. 130. https://doi.org/10.1029/2024JF008085.

Cheng, Q., Tang, C.-S., Xu, D., Zeng, H., Shi, B., 2021. Water infiltration in a cracked soil considering effect of drying-wetting cycles. J. Hydrol. 593. https://doi.org/10.1016/j.jhydrol.2020.125640.

Coppola, A., Gerke, H.H., Comegna, A., Basile, A., Comegna, V., 2012. Dual-permeability model for flow in shrinking soil with dominant horizontal deformation. Water Resour. Res. 48. https://doi.org/10.1029/2011wr011376.

Coppola, A., Comegna, A., Dragonetti, G., Gerke, H.H., Basile, A., 2015. Simulated preferential water flow and solute transport in shrinking soils. Vadose Zone J. 14. https://doi.org/10.2136/vzj2015.02.0021.

Dorduncu, M., Kutlu, A., Madenci, E., Rabczuk, T., 2022a. Nonlocal modeling of bi-material and modulus graded plates using peridynamic differential operator. Eng. Comput. 39, 893–909. https://doi.org/10.1007/s00366-022-01699-2.

Dorduncu, M., Olmus, I., Rabczuk, T., 2022b. A peridynamic approach for modeling of two dimensional functionally graded plates. Compos. Struct. 279. https://doi.org/10.1016/j.compstruct.2021.114743.

Dorduncu, M., Ren, H., Zhuang, X., Silling, S., Madenci, E., Rabczuk, T., 2024. A review of peridynamic theory and nonlocal operators along with their computer implementations. Comput. Struct. 299. https://doi.org/10.1016/j.compstruc.2024.107395.

Dusek, J., Gerke, H.H., Vogel, T., 2008. Surface boundary conditions in two-dimensional dual-permeability modeling of tile drain bromide leaching. Vadose Zone J. 7, 1287–1301. https://doi.org/10.2136/vzj2007.0175.

Dusek, J., Vogel, T., Dohnal, M., Gerke, H.H., 2012. Combining dual-continuum approach with diffusion wave model to include a preferential flow component in hillslope scale modeling of shallow subsurface runoff. Adv. Water Resour. 44, 113–125. https://doi.org/10.1016/j.advwatres.2012.05.006.

Galeandro, A., Doglioni, A., Simeone, V., Šimůnek, J., 2013a. Analysis of infiltration processes into fractured and swelling soils as triggering factors of landslides. Environ. Earth Sci. 71, 2911–2923. https://doi.org/10.1007/s12665-013-2666-7.

Galeandro, A., Šimůnek, J., Simeone, V., 2013b. Analysis of rainfall infiltration effects on the stability of pyroclastic soil veneer affected by vertical drying shrinkage fractures. Bull. Eng. Geol. Environ. 72, 447–455. https://doi.org/10.1007/s10064-013-0492-5.

Gao, Q.-F., Zeng, L., Shi, Z.-N., 2021. Effects of desiccation cracks and vegetation on the shallow stability of a red clay cut slope under rainfall infiltration. Comput. Geotech. 140. https://doi.org/10.1016/j.compgeo.2021.104436.

Gao, Q.-F., Yu, H., Zeng, L., Zhang, R., Zhang, Y.-H., 2023. Roles of vetiver roots in desiccation cracking and tensile strengths of near-surface lateritic soil. Catena 226. https://doi.org/10.1016/j.catena.2023.107068.

Gao, Q.-F., Wu, X.-Y., Zeng, L., Yu, H.-C., Shi, X.-K., 2025. Reliability analysis of soil slope stability considering spatial variability of desiccation cracks. Comput. Geotech. 179. https://doi.org/10.1016/j.compgeo.2024.106977.

Gerke, H.H., Maximilian Köhne, J., 2004. Dual-permeability modeling of preferential bromide leaching from a tile-drained glacial till agricultural field. J. Hydrol. 289, 239–257. https://doi.org/10.1016/j.jhydrol.2003.11.019.

Gerke, H.H., van Genuchten, M.T., 1993. A dual-porosity model for simulating the preferential movement of water and solutes in structured porous media. Water Resour. Res. 29, 305–319. https://doi.org/10.1029/92wr02339.

Gerke, H.H., Dusek, J., Vogel, T., Köhne, J.M., 2007. Two-dimensional dual-permeability analyses of a bromide tracer experiment on a tile-drained field. Vadose Zone J. 6, 651–667. https://doi.org/10.2136/vzj2007.0033.

Gerke, H.H., Dusek, J., Vogel, T., 2013. Solute mass transfer effects in two-dimensional dual-permeability modeling of bromide leaching from a tile-drained field. Vadose Zone J. 12. https://doi.org/10.2136/vzj2012.0091.

Greco, R., Marino, P., Bogaard, T.A., 2023. Recent advancements of landslide hydrology. WIREs Water. https://doi.org/10.1002/wat2.1675.

Greve, A., Andersen, M.S., Acworth, R.I., 2010. Investigations of soil cracking and preferential flow in a weighing lysimeter filled with cracking clay soil. J. Hydrol. 393, 105–113. https://doi.org/10.1016/j.jhydrol.2010.03.007.
Han, X., Islam, A., Abdullah, R.A., 2025. Coupled dual permeability with runoff model for simultaneous analysis of rainfall-induced seepage and runoff. Phys. Fluids 37. https://doi.org/10.1063/5.0250368.
Hencher, S.R., 2010. Preferential flow paths through soil and rock and their association with landslides. Hydrol. Process. 24, 1610–1630. https://doi.org/10.1002/hyp.7721.
Hopp, L., Glaser, B., Klaus, J., Schramm, T., 2020. The relevance of preferential flow in catchment scale simulations: calibrating a 3D dual-permeability model using DREAM. Hydrol. Process. 34, 1237–1254. https://doi.org/10.1002/hyp.13672.
Huang, S., Lu, Z., Ye, Z., Xin, Z., 2020. An elastoplastic model of frost deformation for the porous rock under freeze-thaw. Eng. Geol. 278. https://doi.org/10.1016/j.enggeo.2020.105820.
Jamalinia, E., Vardon, P.J., Steele-Dunne, S.C., 2020. The impact of evaporation induced cracks and precipitation on temporal slope stability. Comput. Geotech. 122. https://doi.org/10.1016/j.compgeo.2020.103506.
Jarvis, N., Koestel, J., Larsbo, M., 2016. Understanding preferential flow in the Vadose Zone: recent advances and future prospects. Vadose Zone J. 15. https://doi.org/10.2136/vzj2016.09.0075.
Khan, M.S., Hossain, S., Ahmed, A., Faysal, M., 2017. Investigation of a shallow slope failure on expansive clay in Texas. Eng. Geol. 219, 118–129. https://doi.org/10.1016/j.enggeo.2016.10.004.
Lade, P.V., 2010. The mechanics of surficial failure in soil slopes. Eng. Geol. 114, 57–64. https://doi.org/10.1016/j.enggeo.2010.04.003.
Laine-Kaulio, H., Backnäs, S., Karvonen, T., Koivusalo, H., McDonnell, J.J., 2014. Lateral subsurface stormflow and solute transport in a forested hillslope: a combined measurement and modeling approach. Water Resour. Res. 50, 8159–8178. https://doi.org/10.1002/2014wr015381.
Larsbo, M., Jarvis, N.J., 2003. MACRO5.0. A Model of Water Flow and Solute Transport in Macroporous Soil. Technical Description.
Lu, N., Şener-Kaya, B., Wayllace, A., Godt, J.W., 2012. Analysis of rainfall-induced slope instability using a field of local factor of safety. Water Resour. Res. 48. https://doi.org/10.1029/2012wr011830.
Luo, Y., Zhang, J.-M., Zhou, Z., Shen, Z.-J., Chong, L., Victor, C., 2021. Investigation and prediction of water infiltration process in cracked soils based on a full-scale model test. Geoderma 400. https://doi.org/10.1016/j.geoderma.2021.115111.
Luo, Y., Zhang, J., Zhou, Z., Aguilar-Lopez, J.P., Greco, R., Bogaard, T., 2023a. Effects of dynamic changes of desiccation cracks on preferential flow: Experimental investigation and numerical modeling. Hydrol. Earth Syst. Sci. 27, 26. https://doi.org/10.5194/hess-27-783-2023.
Luo, Y., Zhang, J., Zhou, Z., Victor, C., 2023b. Modelling preferential flow induced by dynamic changes of desiccation cracks: a comparative numerical study. Geoderma 433. https://doi.org/10.1016/j.geoderma.2023.116471.
Luo, Y., Hou, X., Zhang, J., Wang, Y., Hu, M., Jiang, G., Tang, C.-S., 2025. Exploring the effects of weather-driven dynamics of desiccation cracks on hydrological process of expansive clay slope: insights from physical model test. J. Hydrol. 656. https://doi.org/10.1016/j.jhydrol.2025.133011.
Mualem, Y., 1976. A new model for predicting the hydraulic conductivity of unsaturated porous media. Water Resour. Res. 12, 513–522. https://doi.org/10.1029/WR012i003p00513.
Nieber, J.L., Sidle, R.C., 2010. How do disconnected macropores in sloping soils facilitate preferential flow? Hydrol. Process. 24, 1582–1594. https://doi.org/10.1002/hyp.7633.
Pei, P., Zhao, Y., Ni, P., Mei, G., 2020. A protective measure for expansive soil slopes based on moisture content control. Eng. Geol. 269. https://doi.org/10.1016/j.enggeo.2020.105527.
Pires, L.F., Auler, A.C., Roque, W.L., Mooney, S.J., 2020. X-ray microtomography analysis of soil pore structure dynamics under wetting and drying cycles. Geoderma 362, 114103. https://doi.org/10.1016/j.geoderma.2019.114103.
Reeves, D.M., Parashar, R., Pohlmann, K., Russell, C., Chapman, J., 2014. Development and calibration of dual-permeability flow models with discontinuous fault networks. Vadose Zone J. 13, 1–23. https://doi.org/10.2136/vzj2013.10.0183.
Shao, W., Bogaard, T.A., Bakker, M., Greco, R., 2015. Quantification of the influence of preferential flow on slope stability using a numerical modelling approach. Hydrol. Earth Syst. Sci. 19, 2197–2212. https://doi.org/10.5194/hess-19-2197-2015.
Shao, W., Ni, J., Leung, A.K., Su, Y., Ng, C.W.W., 2017. Analysis of plant root–induced preferential flow and pore-water pressure variation by a dual-permeability model. Can. Geotech. J. 54, 1537–1552. https://doi.org/10.1139/cgj-2016-0629.
Shao, W., Yang, Z., Ni, J., Su, Y., Nie, W., Ma, X., 2018. Comparison of single- and dual-permeability models in simulating the unsaturated hydro-mechanical behavior in a rainfall-triggered landslide. Landslides 15, 2449–2464. https://doi.org/10.1007/s10346-018-1059-0.
Šimůnek, J., Jarvis, N.J., van Genuchten, M.T., Gärdenäs, A., 2003. Review and comparison of models for describing non-equilibrium and preferential flow and transport in the vadose zone. J. Hydrol. 272, 14–35. https://doi.org/10.1016/s0022-1694(02)00252-4.
Smethurst, J.A., Clarke, D., Powrie, W., 2012. Factors controlling the seasonal variation in soil water content and pore water pressures within a lightly vegetated clay slope. Géotechnique 62, 429–446. https://doi.org/10.1680/geot.10.P.097.
SNOW, D.T., 1965. A Parallel Plate Model of Fractured Permeable Media. University of California, Berkeley ProQuest Dissertations Publishing.
Stewart, R.D., Rupp, D.E., Abou Najm, M.R., Selker, J.S., 2016a. A unified model for soil shrinkage, subsidence, and cracking. Vadose Zone J. 15, 1–15. https://doi.org/10.2136/vzj2015.11.0146.
Stewart, R.D., Abou Najm, M.R., Rupp, D.E., Selker, J.S., 2016b. Modeling multidomain hydraulic properties of shrink-swell soils. Water Resour. Res. 52, 7911–7930. https://doi.org/10.1002/2016wr019336.
Stirling, R.A., Toll, D.G., Glendinning, S., Helm, P.R., Yildiz, A., Hughes, P.N., Asquith, J. D., 2021. Weather-driven deterioration processes affecting the performance of embankment slopes. Géotechnique 71, 957–969. https://doi.org/10.1680/jgeot.19.SiP.038.
Sun, D.A., Wang, L., Li, L., 2019. Stability of unsaturated soil slopes with cracks under steady-infiltration conditions. Int. J. Geomech. 19. https://doi.org/10.1061/(asce)gm.1943-5622.0001398.
Take, W.A., Bolton, M.D., 2011. Seasonal ratcheting and softening in clay slopes, leading to first-time failure. Géotechnique 61, 757–769. https://doi.org/10.1680/geot.9.P.125.
Tang, C.-S., Cui, Y.-J., Shi, B., Tang, A.-M., Liu, C., 2011. Desiccation and cracking behaviour of clay layer from slurry state under wetting–drying cycles. Geoderma 166, 111–118. https://doi.org/10.1016/j.geoderma.2011.07.018.
Tang, C.-S., Cheng, Q., Leng, T., Shi, B., Zeng, H., Inyang, H.I., 2020. Effects of wetting-drying cycles and desiccation cracks on mechanical behavior of an unsaturated soil. Catena 194. https://doi.org/10.1016/j.catena.2020.104721.
Tang, Chao-Sheng, Tian, Ben-Gang, Cheng, Qing, Leng, Ting, Bin, Shi, 2024. A comprehensive framework for characterizing and quantifying soil desiccation crack patterns: quantitative parameters and development of CIAS. Eng. Geol. 343, 107820.
Tang, C.-S., Zhu, C., Cheng, Q., Zeng, H., Xu, J.-J., Tian, B.-G., Shi, B., 2021. Desiccation cracking of soils: a review of investigation approaches, underlying mechanisms, and influencing factors. Earth Sci. Rev. 216. https://doi.org/10.1016/j.earscirev.2021.103586.
Tian, B.-G., Cheng, Q., Tang, C.-S., Cui, Y.-J., Wang, H., Shi, B., 2025. Microstructural effects on the tensile strength of a clayey soil during drying: experimental investigation and modelling. Acta Geotech. https://doi.org/10.1007/s11440-025-02774-w.
Tian, B.-G., Cheng, Q., Tang, C.-S., Zeng, H., Xu, J.-J., Shi, B., 2022. Effects of compaction state on desiccation cracking behaviour of a clayey soil subjected to wetting-drying cycles. Eng. Geol. 302. https://doi.org/10.1016/j.enggeo.2022.106650.
Tichavsky, R., Ballesteros-Canovas, J.A., Silhan, K., Tolasz, R., Stoffel, M., 2019. Dry spells and extreme precipitation are the main trigger of landslides in Central Europe. Sci. Rep. 9, 14560. https://doi.org/10.1038/s41598-019-51148-2.
Toll, D.G., Lourenço, S.D.N., Mendes, J., Gallipoli, D., Evans, F.D., Augarde, C.E., Cui, Y. J., Tang, A.M., Rojas, J.C., Pagano, L., Mancuso, C., Zingariello, C., Tarantino, A., 2011. Soil suction monitoring for landslides and slopes. Q. J. Eng. Geol. Hydrogeol. 44, 23–33. https://doi.org/10.1144/1470-9236/09-010.
Uchida, T., Kosugi, K.I., Mizuyama, T., 2001. Effects of pipeflow on hydrological process and its relation to landslide: a review of pipeflow studies in forested headwater catchments. Hydrol. Process. 15, 2151–2174. https://doi.org/10.1002/hyp.281.
Vahedifard, F., Jasim, F.H., Tracy, F.T., Abdollahi, M., Alborzi, A., AghaKouchak, A., 2020. Levee fragility behavior under projected future flooding in a warming climate. J. Geotech. Geoenviron. Eng. 146. https://doi.org/10.1061/(asce)gt.1943-5606.0002399.
van der Spek, J.E., Bogaard, T.A., Bakker, M., 2013. Characterization of groundwater dynamics in landslides in varved clays. Hydrol. Earth Syst. Sci. 17, 2171–2183. https://doi.org/10.5194/hess-17-2171-2013.
van Genuchten, M.T., 1980. A closed-form equation for predicting the hydraulic conductivity of unsaturated soils. Soil Sci. Soc. Am. J. 44, 892–898. https://doi.org/10.2136/sssaj1980.03615995004400050002x.
Wienhöfer, J., Lindenmaier, F., Zehe, E., 2011. Challenges in understanding the hydrologic controls on the mobility of slow-moving landslides. Vadose Zone J. 10, 496–511. https://doi.org/10.2136/vzj2009.0182.
Wilson, G.W., Fredlund, D.G., Barbour, S.L., 1997. The effect of soil suction on evaporative fluxes from soil surfaces. Can. Geotech. J. 34, 145–155. https://doi.org/10.1139/t96-078.
Wu, L., Cheng, P., Zhou, J., Li, S., 2022. Analytical solution of rainfall infiltration for vegetated slope in unsaturated soils considering hydro-mechanical effects. Catena 217. https://doi.org/10.1016/j.catena.2022.106472.
Xie, C., Ni, P., Xu, M., Mei, G., Zhao, Y., 2020. Combined measure of geometry optimization and vegetation for expansive soil slopes. Comput. Geotech. 123. https://doi.org/10.1016/j.compgeo.2020.103588.
Xu, X.-T., Shao, L.-J., Huang, J.-B., Xu, X., Liu, D.-Q., Xian, Z.-X., Jian, W.-B., 2021. Effect of wet-dry cycles on shear strength of residual soil. Soils Found. 61, 782–797. https://doi.org/10.1016/j.sandf.2021.03.001.
Xu, J.-J., Tang, C.-S., Cheng, Q., Vahedifard, F., Liu, B., Shi, B., 2022. Monitoring and early detection of soil desiccation cracking using distributed fibre optical sensing. Géotechnique 1-12. https://doi.org/10.1680/jgeot.21.00397.
Xu, J.J., Tang, C.S., Yang, Y., Li, L., Zhang, H., Cheng, Q., Zhang, X.Y., Liu, B., Shi, B., 2024. Breathing phenomenon of soil desiccation cracking: insights from novel geophysical observations. Case Rep. Med. 129. https://doi.org/10.1029/2023jf007318.
Xue, Y., Miao, F., Wu, Y., Dias, D., 2022. Dynamic stability assessment of reservoir colluvial landslide using a hypoplastic clay constitutive model considering the effects of drying-wetting cycles on the hydro-fluctuation belt. Eng. Geol. 307. https://doi.org/10.1016/j.enggeo.2022.106791.
Yang, Z.-M., Tang, C.-S., Wang, T., Cheng, Q., Liu, J.-D., Zeng, Z.-X., Shen, Z., 2025. Generating and predicting soil desiccation cracking patterns utilizing a stochastic model based on geometric parameters. Eng. Geol. 353. https://doi.org/10.1016/j.enggeo.2025.108122.
Yuliana, Y., Apriyono, A., Kamchoom, V., Boldrin, D., Cheng, Q., Tang, C.-S., 2025. Seasonal dynamics of root growth and desiccation cracks and their effects on soil

hydraulic conductivity. Eng. Geol. 349. https://doi.org/10.1016/j.enggeo.2025.107973.
Zeng, H., Tang, C.S., Zhu, C., Cheng, Q., Lin, Z.Z., Shi, B., 2021. Investigating soil desiccation cracking using an infrared thermal imaging technique. Water Resour. Res. 58. https://doi.org/10.1029/2021wr030916.
Zhan, T.L.T., Chen, R., Ng, C.W.W., 2013. Wetting-induced softening behavior of an unsaturated expansive clay. Landslides 11, 1051–1061. https://doi.org/10.1007/s10346-013-0449-6.
Zhang, J., Zhu, D., Zhang, S., 2020. Shallow slope stability evolution during rainwater infiltration considering soil cracking state. Comput. Geotech. 117. https://doi.org/10.1016/j.compgeo.2019.103285.
Zhang, J.-M., Luo, Y., Zhou, Z., Victor, C., Duan, M., 2021a. Research on the rainfall-induced regional slope failures along the Yangtze River of Anhui, China. Landslides 18, 1801–1821. https://doi.org/10.1007/s10346-021-01623-7.
Zhang, J.-M., Luo, Y., Zhou, Z., Chong, L., Victor, C., Zhang, Y., 2021b. Effects of preferential flow induced by desiccation cracks on slope stability. Eng. Geol. 288. https://doi.org/10.1016/j.enggeo.2021.106164.
Zhang, H., Yang, J., Wang, L., Xu, Y., 2022a. Model test on the dynamic characteristics of crack formation in expansive soil slopes under alternate drying and wetting. Acta Geotech. https://doi.org/10.1007/s11440-022-01700-8.
Zhang, Y., Zhao, D., Zheng, Q., Huang, Y., Jiang, F., Wang, M.-K., Lin, J., Huang, Y., 2022b. Evaluating the effects of temperature on soil hydraulic and mechanical properties in the collapsing gully areas of South China. Catena 218. https://doi.org/10.1016/j.catena.2022.106549.
Zhou, X., Hu, J., Wei, Y., Cai, C., 2021. Estimation of soil detachment capacity on steep slopes in permanent gullies under wetting-drying cycles. Catena 206. https://doi.org/10.1016/j.catena.2021.105450.
Zhuang, X., Ren, H., Rabczuk, T., 2021. Nonlocal operator method for dynamic brittle fracture based on an explicit phase field model. Eur. J. Mech. A. Solids 90. https://doi.org/10.1016/j.euromechsol.2021.104380.
Zhuang, X., Zhou, S., Huynh, G.D., Areias, P., Rabczuk, T., 2022. Phase field modeling and computer implementation: a review. Eng. Fract. Mech. 262. https://doi.org/10.1016/j.engfracmech.2022.108234.